University of Alberta

DISPERSED BUBBLE AND PARTICULATE FLOWS IN LIQUID CONTINUOUS MEDIA

by

Divya Kumar ©

A thesis submitted to the Faculty of Graduate Studies and Research in partial fulfillment of the requirements for the degree of **Master of Science**.

in

Chemical Engineering

Department of Chemical and Materials Engineering

Edmonton, Alberta
Fall 2006

Reproduced with permission of the copyright owner. Further reproduction prohibited without permission.

Library and Archives Canada

Published Heritage Branch

395 Wellington Street
Ottawa ON K1A 0N4
Canada

Bibliothèque et Archives Canada

Direction du Patrimoine de l'édition

395, rue Wellington
Ottawa ON K1A 0N4
Canada

Your file Votre référence
ISBN: 978-0-494-22300-0
Our file Notre référence
ISBN: 978-0-494-22300-0

NOTICE:
The author has granted a non-exclusive license allowing Library and Archives Canada to reproduce, publish, archive, preserve, conserve, communicate to the public by telecommunication or on the Internet, loan, distribute and sell theses worldwide, for commercial or non-commercial purposes, in microform, paper, electronic and/or any other formats.

The author retains copyright ownership and moral rights in this thesis. Neither the thesis nor substantial extracts from it may be printed or otherwise reproduced without the author's permission.

AVIS:
L'auteur a accordé une licence non exclusive permettant à la Bibliothèque et Archives Canada de reproduire, publier, archiver, sauvegarder, conserver, transmettre au public par télécommunication ou par l'Internet, prêter, distribuer et vendre des thèses partout dans le monde, à des fins commerciales ou autres, sur support microforme, papier, électronique et/ou autres formats.

L'auteur conserve la propriété du droit d'auteur et des droits moraux qui protège cette thèse. Ni la thèse ni des extraits substantiels de celle-ci ne doivent être imprimés ou autrement reproduits sans son autorisation.

In compliance with the Canadian Privacy Act some supporting forms may have been removed from this thesis.

While these forms may be included in the document page count, their removal does not represent any loss of content from the thesis.

Conformément à la loi canadienne sur la protection de la vie privée, quelques formulaires secondaires ont été enlevés de cette thèse.

Bien que ces formulaires aient inclus dans la pagination, il n'y aura aucun contenu manquant.

Canada

Reproduced with permission of the copyright owner. Further reproduction prohibited without permission.

Abstract

Oil sand hydrotransport is used to transport and condition oil sand ore. These mixtures contain sand, clays, bitumen, water and air. This study looks at a method to measure air bubble size distributions in an opaque medium and presents a semi-empirical single fluid Eulerian model for turbulent slurry (solid-liquid) flows.

A piston sampler was used to grab a small sample from pipeline. Bubbles contained in the sample are released into a water-filled tube so that bubble images can be captured. Results showed that the piston sampler did not provide an accurate measurement of the in situ bubble size distribution.

The model uses a new quantity, turbulent slurry viscosity, to predict frictional pressure drops and concentration profiles for slurries of fine particles ($< 250\mu m$) at flow velocities greater than the deposition velocity. Model predictions were in satisfactory agreement with results obtained from the literature.

Reproduced with permission of the copyright owner. Further reproduction prohibited without permission.

Acknowledgements

First of all I would like to thank my supervisors, Dr. K. Nandakumar and Dr. Sean Sanders for their constant support and encouragement throughout my stay. I would also like to thank Artin for always helping me out with the experiments. I would like to specially thank Dr. J. H. Masliyah for his guidance and support at critical times. I have enjoyed the company and the interesting discussions with my colleagues from the extraction and the computational group at room 668. I also want to thank my regular squash buddies, Nakeeran, Siddharth and Mahesh for always giving me an entertaining break. Then last not least, Ma, Pa, Appu and Mahesh for their love and support.

Reproduced with permission of the copyright owner. Further reproduction prohibited without permission.

Contents

Reproduced with permission of the copyright owner. Further reproduction prohibited without permission.

Reproduced with permission of the copyright owner. Further reproduction prohibited without permission.

List of Tables

Reproduced with permission of the copyright owner. Further reproduction prohibited without permission.

List of Figures

Reproduced with permission of the copyright owner. Further reproduction prohibited without permission.

Reproduced with permission of the copyright owner. Further reproduction prohibited without permission.

Nomenclature

α	Penalty Parameter
ε	Turbulence Dissipation, m^2/s^3
ε_s	Turbulent Diffusivity, m^2/s
η	Kolmogorov Length Scale, m
γ_{ij}	Shear Rate
μ	Suspension Shear Viscosity, kg/m/s
μ_f	Carrier Phase Shear Viscosity kg/m/s
μ_r	Relative Suspension Viscosity
μ_t	Turbulent Viscosity of Slurry, kg/m/s
ν_f	Kinematic Viscosity of Carrier Phase, m^2/s
ν_{tf}	Turbulent Viscosity of Carrier Fluid
ν_{tm}	Turbulence Modulation due to addition of particles
ν_{tp}	Particle Concentration Effect on Turbulent Slurry Viscosity
ν_{ts}	Dimensionless Turbulent Viscosity of Slurry
Ω	2-D Pipeline Cross-Section
Φ	In-situ Concentration of Particles
Φ_m	Maximum Packing Fraction of Particles
Φ_p	Average Concentration of Particles
ρ_d	Density Difference relative to Fluid Density
ρ_f	Carrier Phase Density, kg/m^3
ρ_p	Particle Density, kg/m^3

Reproduced with permission of the copyright owner. Further reproduction prohibited without permission.

τ Kolmogorov Time Scale, s

τ_{pL} Particle Integral Time Scale, s

τ_p Relaxation Time of Particle, s

Υ Shear Rate, s^{-1}

b_i Fitted Parameters in the Model

C_D Drag Coefficient

d_{50} Mean Particle Size of Slurry, m

d_b Diameter of Bubbles, m

D_{damp} Turbulence Dampening factor

d_p Diameter of Particle, m

D_{tpdx1} Particle Turbulent diffusivity in x_1-direction

D_{tpdx2} Particle Turbulent diffusivity in x_2-direction

D_{tppx1} Diffusivity due to Particle-Particle Interaction in x_1-direction

D_{tppx2} Diffusivity due to Particle-Particle Interaction in x_2-direction

D_{tpx1} Overall Particle Diffusivity in x_1-direction

D_{tpx2} Overall Particle Diffusivity in x_2-direction

D_t Pipeline Diameter, m

Fr_s Froude Number for Scale-up

L_e Eulerian Length Scale, m

N_G Gravitational Flux

Re_p Particle Reynolds Number

t_c Crossover Time from one Eddy to another, s

T_L Integral Time Scale of Eddies, s

$u_p'^2$ Particle Fluctuation Velocity, m^2/s^2

U_{avg} Mean Flow Rate, m/s

u_i Velocity in i-Direction, i=1,2,3

V_g Particle Drift Velocity in Eddy, m/s

Reproduced with permission of the copyright owner. Further reproduction prohibited without permission.

V_t	Hindered Settling velocity, m/s
x_i	Position in i-Direction, i=1,2,3
A	Projected Area of the Bubble, m^2
BSD	Bubble Size Distribution
CFD	Computational Fluid Dynamics
CHWE	Clark Hot Water Extraction
CTE	Cross Trajectory Effect
cte	Cross Trajectory Effect
f	Correction factor for Hindrance
fps	Frames Per Second
Fr	Froude Number
g	Gravity, m/s^2
HIST	Homogenous Isotropic Steady Turbulence
IE	Inertia Effect
K	Dimensionless Pressure Drop Constant
L	Characteristic Length, m
p	Pressure
PBM	Population Balance Model
Q	Flow Rate
Re	Reynolds Number
S	Stokes Number
SRC	Saskatchewan Research Council
U	Characteristic Velocity, m/s
U_c	Deposition Velocity m/s
W	Axial Flow Velocity, m/s

Reproduced with permission of the copyright owner. Further reproduction prohibited without permission.

Chapter 1

Introduction

Slurry transport has been in use for long distance transport of materials like coal, mineral concentrates, ore and tailings. Nowadays, slurry transport is being used by the oil sands industry to transport oil sands from mining to extraction site and to dispose the tailings produced during oil sands extraction. The present-day extraction processes used by most of the companies are based on Clark Hot Water Extraction (CHWE) (Masliyah et al., 2004). Figure 1.1 shows a schematic of a typical extraction process. Oil sand ore after being mined and crushed is mixed with process water in mixing boxes to prepare the slurry. The oil sand slurry is then hydrotransported in pipelines to the extraction site. During hydro-transportation oil sand lumps are further broken down and bitumen is also released from oil sand ore. The slurry from the pipeline may then be aerated to promote bitumen-air attachment. The bitumen froth is then separated from slurry using large gravity separation vessels. These processes constitute a typical bitumen extraction process from oil sands.

The hydrotransport pipelines operate in the turbulent regime, hence there is a lot of shear in the pipeline. This high shear environment in the pipeline helps in breaking the oil sand lumps and in digestion of the ore i.e. release of bitumen from oil sands. By injecting air in the pipeline, it has been shown in laboratory tests (Wallwork, 2003; Luthra et al., 2004), that bitumen recovery increases at low process temperatures ($< 50°C$). Further, Malysa et al. (1999) showed that bitumen droplets tend to attach to air bubbles of similar size. Thus, it is important to understand the coalescence and breakup mechanisms that determine the equilibrium bubble size

Reproduced with permission of the copyright owner. Further reproduction prohibited without permission.

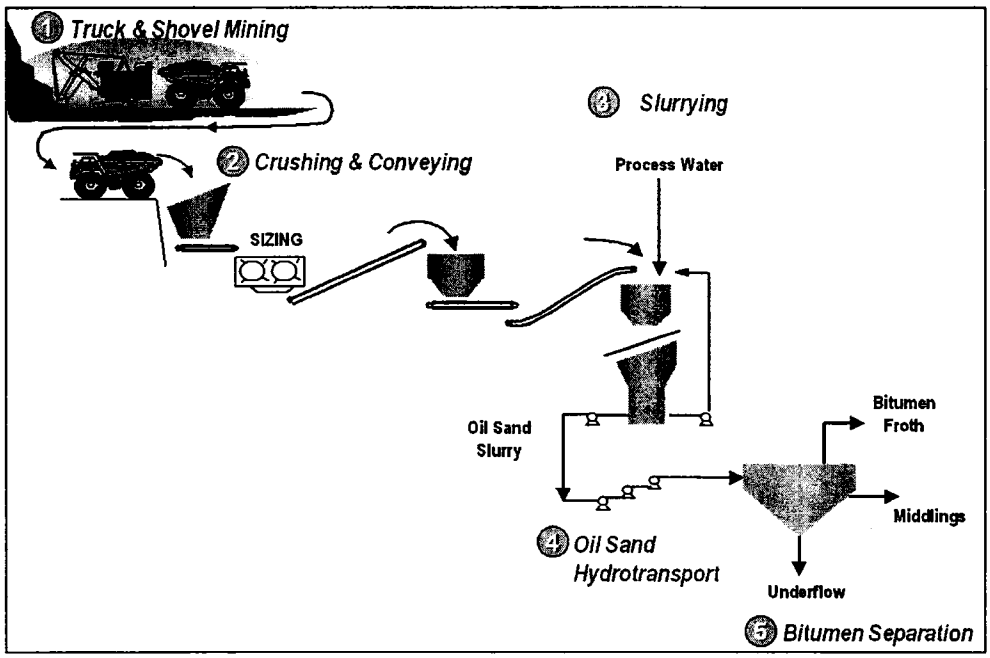

Figure 1.1: Schematic of Extraction Process (Sanders et al., 2002)

distribution under pipeline flow conditions. These pipelines operate at high sand concentrations (> 30% by volume), and hence pose an extremely challenging environment to measure the in-situ Bubble Size Distribution (BSD).

There is a dearth of literature concerning air-slurry flows in pipelines. Most of the multiphase studies reported to date pertain to two phase flows i.e. gas-liquid, solid-liquid, liquid-liquid and gas-solid. Books by Wallis (1969) and Govier and Aziz (1972) have reviewed two-phase flows in both vertical and horizontal pipelines and provide flow maps, friction factors for pressure drop calculations and hold-up correlations. This work investigates the transport of three phases viz. air, sand and water in pipeline.

Due to the challenging nature of studying air-slurry flows through pipelines, it has been further divided into two-phase flows viz. air-water and sand-water flows in pipelines. In gas-liquid flows a considerable amount of experimental and modeling work has been done to study BSD. Hesketh et al. (1987, 1991a,b) experimentally studied bubble break-up and predicted maximum bubble size occurring in turbulent air-water flows through small diameter pipes. Martinez-Bazan et al. (1999a,b) and

Reproduced with permission of the copyright owner. Further reproduction prohibited without permission.

Lasheras et al. (2001) have modeled BSD using population balance models (PBM). The distribution is governed by the equilibrium between dispersed phase break-up and coalescence. In turbulent flows, phenomena affecting break-up determine the smallest bubble size and coalescence determines the maximum bubble size. The PBM developed by Prince and Blanch (1990) in bubble columns is a widely used model and has also been incorporated in Computational Fluid Dynamics(CFD) software like ANSYS-CFX.

Due to the practical application of solid-liquid transport using pipelines, a lot of experimental work has been done primarily to determine pressure drops and minimum operating velocities. On the modeling aspect, most of the work, (empirical or mechanistic) has been to predict head loss and settling velocity. The book by Shook and Roco (1991) provides a comprehensive review on slurry transport. Many experimental studies of slurry flow have been conducted at the Saskatchewan Research Council (SRC), such as Schaan et al. (2000) and Gillies et al. (2004).

In the experimental studies conducted at the University of Alberta, BSD has been measured successfully in air-water systems using an imaging technique (Razzaque et al., 2003; Sanders et al., 2004). They photographed bubbles flowing in the pipeline and measured BSD using the projected area of the bubbles. The results of this technique agree well with the theory and previous experimental studies. However, on addition of particles to the flow, the medium becomes opaque and photographic technique fails. To overcome this problem a different technique has been adapted from one used by Syncrude Canada Ltd. to study BSD in slurry pipelines. In the new design a small volume of the flow mixture containing the bubbles is grabbed from the pipeline, which is then analysed to measure the BSD using a photographic technique. Part of the objective of this study is to compare BSD measured by the new technique with the old photographic technique employed by Razzaque et al. (2003).

Eskin et al. (2004) have discussed the effects of interactions between particles and bubbles on bubble breakup and coalescence models. To successfully model air-slurry systems in pipeline flows, it is important to understand slurry flows. With the advent of powerful computing machines and CFD software, slurry flow modeling

Reproduced with permission of the copyright owner. Further reproduction prohibited without permission.

might appear a trivial task. But the models incorporated for particle dispersion phenomena were originally derived for different flow geometry and applications like fluidisation. The main feature of this study is the handling of particle dispersion. A 2-D slurry flow model has been developed to study the effects of particle shape, size, density and concentration, carrier phase properties, turbulence levels and pipeline diameter on particle dispersion and frictional pressure drop. The model, though having limitations in comparison with experimental results, can in future be applied to 3-D model of slurry flows in CFD software. Thus, the objectives of the thesis can be summarised as follows:

1. To measure bubble size distribution in air-water-sand flows in pipelines.
2. To model concentration profile and pressure drop measurements in slurry pipelines.

The thesis has been divided as following:

- A review of the literature on modeling of sand-water flows and experimental techniques used in multiphase flows to determine bubble or particle size, hold-up and in-situ velocities has been discussed in Chapter 2
- Design of experimental setup and testing of the piston sampler as a BSD measuring technique has been discussed in Chapter 3
- Development and validation of slurry flow model has been discussed in Chapter 4
- A discussion on future work is presented in Chapter 5

Reproduced with permission of the copyright owner. Further reproduction prohibited without permission.

Chapter 2

Literature Review

2.1 Measurement of air BSD in slurry pipelines

In the previous study, Razzaque et al. (2003) used an imaging technique to measure the BSD in air-water flows at low water velocities. The flow was observed to be in coalescence dominant regime and BSD showed a log-normal distribution at velocities higher than 2.9 m/s. The maximum bubble size measured agreed well with the Levich breakup theory (Hesketh et al., 1991a,b).

On adding sand particles to the flow, the fluid became opaque making bubble recognition via the photographic technique immensely difficult. Figure 2.1 shows images of bubbles on addition of particles. It shows that the opacity of the medium increases rapidly with the particle concentration. Hence, bubble size cannot be measured using the photographic technique even at a low solids concentration of 0.5%. A new technique has to be devised to measure the steady state BSD in the pipeline at high concentration of particles. The new technique should allow one to differentiate between particles and bubbles. Several experimental techniques have been reported to measure phase distribution, phase velocities, dispersed phase characterisation and pressure drop in multiphase flows. These techniques can be divided as intrusive and non-intrusive techniques (Boyer et al., 2002). Invasive methods are commonly used for measuring in-situ properties like local, time averaged velocity and concentration.

Reproduced with permission of the copyright owner. Further reproduction prohibited without permission.

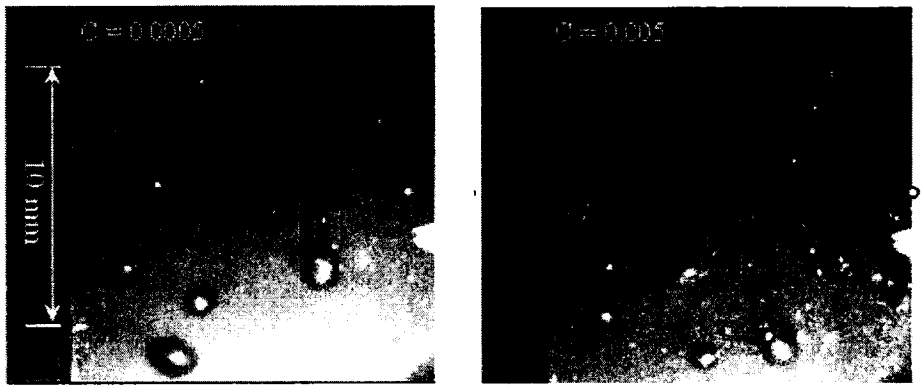

(a) Φ_p=0.0005 (b) Φ_p=0.005

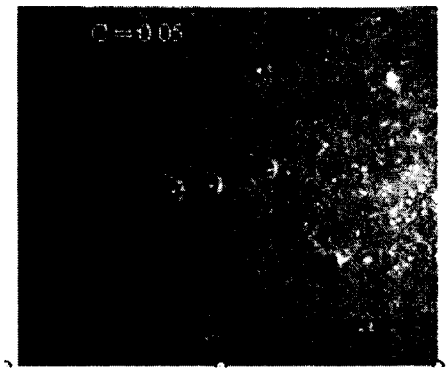

(c) Φ_p=0.05

Figure 2.1: Bubbles as viewed upon addition of solids

2.1.1 Photographic Techniques

Photographic techniques are the simplest of techniques and so have been adopted by several researchers (Malysa et al., 1999; Chen et al., 2001) to measure BSD. Saxena et al. (1988) provide a good review of the experiments that have used photographic techniques to measure BSD. Bubble images are taken using cameras, which are then processed and analysed to compute the BSD. The technique requires the medium and walls to be transparent and bubbles must appear near the photographing wall. In three phase flows, by matching the refractive index of solids and liquid, BSD can be measured (Boyer et al., 2002). This technique does not have any spatial resolution, but gives BSD across the sampled cross section.

Reproduced with permission of the copyright owner. Further reproduction prohibited without permission.

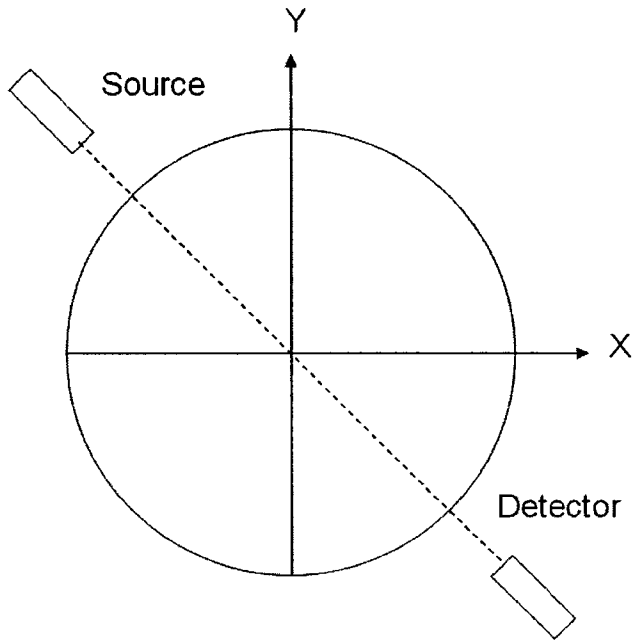

Figure 2.2: A cross section being scanned by tomographic sensor

2.1.2 Tomographic Techniques

The principle of tomographic techniques like X-ray, $\gamma-$ ray and ultrasonic measurement techniques is to measure a physical property which is dependent on the phase hold-up. As shown in Figure 2.2 a tomographic sensor is used to scan the circular cross-section. A tomographic sensor has a source from which it sends a X-ray or any other signal that can pass through fluid and pipe walls. The signal is detected at the other end by the detector. The attenuation which the signal undergoes is then used to determine the average phase concentration along that particular path traveled by the signal. To obtain concentration over the whole cross-section, both the source and detector have to rotate simultaneously through out the cross-section, which means that sensor should rotate fast before any significant changes occurs in the cross-section (Boyer et al., 2002). Thus, these sensors only provide averaged values along the chord traveled by the signal and moreover measurements are also time averaged. Recently, electrical tomography has been used by Prasser et al. (2001) to measure BSD of gas-liquid flows in vertical columns. A set of wire-mesh sensors (Prasser et al., 1998) was used to measure the conductivity across

Reproduced with permission of the copyright owner. Further reproduction prohibited without permission.

the cross-section which was related to the gas-fraction. The sensors do break the bubbles but provide a measure of the bubble sizes before they break. As all the sensors act simultaneously, this measurement provides a high spatial resolution at any instant in time.

2.1.3 Capillary Suction Probe

Tucker et al. (1994) have used a capillary suction probe to determine BSD in flotation cells containing slurries of sand concentrations of 30% weight fraction. The design of the capillary suction is described in Barigou and Greaves (1991). Bubbles are separated from the slurry into a water solution with the same chemistry as in the flotation cell where they are measured using a bubble size analyser. The bubbles were separated using a tubular device with an orifice at the bottom, with the diameter of the orifice being four times that of the expected maximum bubble diameter. Segregation in the capillary during bubble suctioning is a problem (Chen et al., 2001).

2.1.4 Intrusive Measurements using Probes

Probes are thin and sharp ended needles facing the flow direction (Boyer et al., 2002). Different kinds of probes have been developed such as optical, impedance, thermal and electrochemical. The principle behind these probes is similar to the tomographic technique, where optical probes measure an optical property and impedance probes measure an electrical property locally, which is then related to the volumetric fraction of the dispersed phase. These probes can be used to measure volumetric concentration of phase, dispersed phase velocity and size and time-averaged local interfacial area (Cartelier and Achard, 1991; Boyer et al., 2002). Single probes give information about the phase concentration only. To get more information on size distribution of dispersed phase, multiple probes are used (Saxena et al., 1988; Boyer et al., 2002). The time difference between the signals received by the probes allows measurements of bubble velocity and size. Amongst the various probes mentioned, optical and impedance probes have been used to measure bubble sizes in multiphase flows. Both optical and impedance probes continuously deliver signals which carry

Reproduced with permission of the copyright owner. Further reproduction prohibited without permission.

information about the phase distribution. The signals received by both the probes are analysed using signal processing tools. A good review of the theory behind probe operation, its design and calibration and signal processing tools are given by Cartelier and Achard (1991). Ishida and Tanaka (1982) have used optical probes to measure bubble size in 3-phase systems, but with low solids concentrations. De-Lasa et al. (1984) have used a U-shaped optical fibre to measure bubble size in 3-phase fluidised beds. Matsuura and Fan (1984) designed a two-electrode resistivity probe to study bubble properties in 3-phase fluidised beds. Due to the invasive nature of probes their interaction with bubbles can not be neglected. The probe has to be thin compared to the bubble sizes under consideration (Boyer et al., 2002). By using multiple probes the design can become bulky (Saxena et al., 1988); thus interactions with the bubbles becomes significant.

Most of the experimental techniques for measuring BSD that are reviewed here have limitations in their applicability to the current set-up. Photographic techniques have been reported to have problems at high sand concentration (Chen et al., 2001). Electrical tomographic technique developed by Prasser et al. (2001) has not been tested in three-phase flows and it is difficult to comment whether it will work with the existing set-up. However, tomographic techniques might be applied to the current set-up if it can be modified in the same way as electrical tomography to provide a high spatial resolution and faster measurement rates. The capillary suction probe measures bubble sizes after bubbles have been separated from the slurry, thus the problem of separating bubbles from the slurry still persists. Due to the small diameter of existing pipeline (ID of 25.4mm), intrusive measurements are expected to interfere with the bubble sizes and hydrodynamics of the flow. Thus, it can lead to measurement of erroneous BSD.

A new experimental design has been adapted from Syncrude Canada Ltd. The piston sampler has been found to be useful in industrial scale pipeline. The piston sampler grabs a small sample from the pipeline and releases it in a column of water, in which sand particles settle and air bubbles rise. A photographic technique is then used to measure the bubble sizes in the water column. The piston sampler has been tested in a laboratory scale pipeline as a BSD measurement technique in the current

Reproduced with permission of the copyright owner. Further reproduction prohibited without permission.

study.

2.2 Slurry Flow Modeling

At steady state, fully developed flow in a pipeline has an equilibrium between bubble coalescence and breakup rates, which results in a stable configuration of BSD. The BSD in air-water flows can be predicted if appropriate breakup and coalescence models are used in conjunction with turbulence models. As we move on from air-water systems to air-slurry systems, it becomes more challenging to predict the BSD. By adding particles to air-water systems, bubbles start colliding with particles also. Hence, the breakup rate of bubbles increases, thereby reducing the mean bubble size, as has been observed by Razzaque et al. (2003). The increase in breakup rate depends on particle size, density and concentration (Eskin et al., 2004). Moreover, by adding particles, the fluid turbulence structure changes, which is known as turbulence modulation. Turbulence modulation depends on particle size, density and concentration and carrier fluid velocity (Crowe et al., 1996; Kenning and Crowe, 1997; Crowe, 1999). Thus, knowledge of particle size distribution and turbulence structures in a slurry pipeline is important to estimate BSD.

A lot of early research on slurry flows focused on deriving empirical relations for deposition velocity and pressure drop. These correlations have been comprehensively reviewed in Shook and Roco (1991). Empirical relations were followed by macroscopic modeling i.e. two-layer models based on force and mass balances between the layers (Shook and Roco, 1991). Both empirical relations and macroscopic modeling were based on the settling tendency of slurries. Settling nature, as the name suggests, is determined by the settling velocity of the particles in a still fluid. This is dependent on the particle and fluid bulk properties. Non-settling slurries are known as homogenous slurries as they are uniformly dispersed in the slurry due to their non-settling nature. Settling or heterogenous slurries have asymmetric concentration and velocity profiles. A part of the friction to the flow is "Coulombic" in nature i.e. it is velocity independent and is caused by the immersed weight of particles not fully suspended by turbulence (Shook et al., 2002).

Reproduced with permission of the copyright owner. Further reproduction prohibited without permission.

2.2.1 Microscopic Modeling

Two-phase flows with solids as the dispersed phase in liquid or gas as the continuous phase can be modeled using the Lagrangian or Eulerian approach. In the Lagrangian approach, each particle trajectory is tracked by solving Newton's law of motions for the particle, including all of the external forces acting on the particle. However, the effect of the particles on the fluid is often ignored. Hence for higher solids loading this technique is not useful (Hsu et al., 1989; Crowe et al., 1996). In the Eulerian approach particles are treated as a continuum over a volume averaged scale. Flow properties are solved using bulk properties of the particles and a momentum equation for each phase (Hsu et al., 1989; Crowe et al., 1996). Most of the industrial applications of slurry pipelines have a dense flow of solids under turbulent conditions and thus a Eulerian approach is more suitable. In the Eulerian approach, there are two ways to formulate the equations of motion:

Two-fluid Model: Both solids and carrier fluid are treated as separate phases. Separate momentum equations for both phases are solved with appropriate closure models to account for phase interactions. Formulations using this approach have been developed by Pourahmadi and Humphrey (1983); Hsu et al. (1989) and Ling et al. (2003).

Single Fluid Model: The slurry is treated as a single phase. The slurry bulk properties incorporate the effects of particle size, shape and volume fraction. The single phase momentum equation is solved along with a convection-diffusion equation for the dispersed phase. Most of the work in this area has been done by Roco and Shook (1983, 1985). They have used this approach to solve slurry flow of a particulate mixture containing particles of N-different diameters.

In a single fluid model, the physical phenomena governing the momentum balance in the carrier fluid are well established; however, particle transport is still challenging. The particles in the current study are always presumed to be negatively buoyant. Thus, particles have a tendency to settle in the direction of gravity. The phenomena dispersing the particles and gravitational flux have been commonly

Reproduced with permission of the copyright owner. Further reproduction prohibited without permission.

analysed only in one direction viz. the direction of gravity, which has been represented by x_2 in this study. The convection-diffusion equation is widely used to model particle transport as shown in Equation 2.1:

$$\varepsilon_s \frac{d\Phi}{dx_2} + V_t \Phi = 0 \tag{2.1}$$

where ε_s is analogous to turbulent kinematic viscosity and V_t is the hindered settling velocity (Gillies, 1993). In equation 2.1, the gravitational flux (second term on left hand side) is balanced with turbulent dispersion (first term on the left hand side) in x_2-direction. Equation 2.1 does not incorporate particle-particle interaction effects, which have been observed by Shook and Daniel (1965) and modeled by Roco and Shook (1983).

Roco and Shook (1983) and Shook and Roco (1991) have used a force balance approach to model the concentration profile of sand-water mixtures. They balanced the gravitational force with turbulent dispersion and inter-particle force. The inter-particle force was divided into three parts: particle dispersion due to their fluctuating velocities, Bagnold dispersive force and Coulombic forces between the pipe wall and particles. The first force arises due to the interaction of particles because of the turbulent fluctuations experienced by them. Bagnold dispersive force is another dispersive force which repels particles from each other under shear flow (Bagnold, 1954, 1956), in which two different regimes have been identified viz. macroviscous (viscous force dominant) and particle-inertia (particle inertia dominant). Holtham (1992) has explained the two regimes in detail. Coulombic force is the normal dispersive force from the wall experienced by particles if they tend to form a bed at the bottom (Roco and Shook, 1983).

The model of Roco and Shook (1983) provides reasonable predictions of concentration distribution for particle size ranging between $165\mu m < d_p < 13mm$ and $\Phi < 0.4$. Hsu et al. (1989) have also developed a two-dimensional model, but for multi component species, by modifying the underlying theme of Roco and Shook (1983). They included the effect of Saffman lift force to model the dispersed phase. Their model shows good agreement even for larger particles.

Reproduced with permission of the copyright owner. Further reproduction prohibited without permission.

Roco and Shook (1983) have also used a single phase momentum equation for slurry, in which turbulent stresses were empirically related to the partial derivative of turbulent kinetic energy of the slurry. Over the years Roco and coworkers (Roco and Balakrishnan, 1983; Roco and Mahadevan, 1986) have modified the turbulence modeling and used higher order turbulence models for a better estimate of eddy viscosity. Roco and Mahadevan (1986) used a one equation kinetic energy model for turbulent viscosity. The model provides good predictions; however, there are many empirical parameters. Hsu et al. (1989) introduced an axial slip velocity for the particles and used an algebraic equation for eddy viscosity.

The critical point in slurry flow modeling has been the force balance for the dispersed phase. Thus it is important to review the various mechanisms of particle dispersion both in laminar and turbulent slurry flows.

2.2.2 Turbulent Dispersion

To model particle dispersion we need deterministic information on turbulence in the carrier fluid, which is still not provided by the turbulence models as most of them are based on stochastic models. In turbulent flows, contrary to laminar flows, the fluid moves in a random way. This randomness is termed as turbulence and has been modeled by many researchers using probabilistic models. Turbulent motion is characterised by the presence of small rotating structures called eddies. Particles in a turbulent fluid are transported by these eddies, and this phenomenon is called turbulent particle dispersion.

Due to the complexity involved in modeling turbulence, turbulence is commonly assumed to be homogenous, i.e. it is independent of the position, isotropic, i.e. independent of the direction, and steady. The combination of these factors is called homogenous isotropic steady turbulence (HIST). Turbulent flow consists of cascades of eddies. Each eddy is associated with a length and time scale. The larger eddies with higher inertia do not respond to viscous forces , thus they break into smaller eddies until viscous forces become dominant and these smaller eddies then dissipate their energy (Shirolkar et al., 1996). The length and time scale of the

Reproduced with permission of the copyright owner. Further reproduction prohibited without permission.

smallest eddy is given by the Kolmogorov relations (Equations 2.2):

$$\eta = (\frac{\nu_f^3}{\varepsilon})^{1/4} \tag{2.2a}$$

$$\tau = (\frac{\nu_f}{\varepsilon})^{1/2} \tag{2.2b}$$

where η and τ are Kolmogorov length and time scale for the smallest eddy. ν_f and ε are turbulent viscosity and dissipation respectively. Similarly length and time scale of largest possible eddy is called integral length (L_e) and time scale (T_L) of fluid. The integral length scale depends on the geometry of the fluid flow and integral time scale is the time for which eddy velocity can be correlated to its initial velocity, i.e. the time for which the initial velocity of the eddy will have an effect on the velocity of eddy (Mols and Oliemans, 1998; Shirolkar et al., 1996).

A particle that is added to the carrier fluid can be carried by eddies larger than the particle. Thus particles have been classified as small, medium and large depending on their size relative to the range of eddy sizes. A particle is small if its size is smaller than η as given in Equation 2.2; medium if it lies between η and L_e; and large if particle is greater than L_e (Shirolkar et al., 1996). This classification determines the range of eddies which can carry a given particle size. A single small particle in HIST will be carried by all the eddies, as its size is smaller than η. Thus it will stay in an eddy until the eddy dissipates or breaks.

Particles can also be classified on the basis of Stokes Number (S). Stokes Number is defined as ratio of relaxation time of particle to T_L. Relaxation time can be understood as the response time of a particle to fluctuations in the flow. It is given by the following relation :

$$\tau_p = \frac{24\rho_p d_p^2}{18\mu_f C_D Re_p} \tag{2.3a}$$

where Re_p is Reynolds Number of particle based on the relative velocity of particle with respect to the fluid, C_D is given by

$$C_D = \frac{24}{Re_p}(1+0.15Re_p^{0.687}) \text{ for } Re_p < 10^3 \tag{2.3b}$$

Reproduced with permission of the copyright owner. Further reproduction prohibited without permission.

thus for a particle in Stokes regime ($Re_p \ll 1$) is given by:

$$\tau_p = \frac{\rho_p d_p^2}{18 \nu_f \rho_f} \tag{2.3c}$$

and Stokes Number is given by equation 2.4 as follows:

$$S = \frac{\tau_p}{T_L} \tag{2.4}$$

If $S < 1$, a particle would have the same fluctuations as the fluid; for $S \sim 1$, a particle will experience slightly different fluctuations from the fluid and for $S > 1$, particle will experience dampened fluctuations at fluid-particle interface. Thus the inertia of particles reduces the fluctuations experienced by a particle as compared to that of eddy and this effect of inertia is called INERTIA EFFECT.

Another important property of a particle is its free fall velocity, which causes the particle to move with a drift velocity (V_g) within the eddy, i.e. difference of particle and fluid velocity. Thus if the time taken to traverse the eddy length is less than eddy lifetime then particle migrates to another eddy. This is called CROSS TRAJECTORY EFFECT. It can also be defined as the ratio of T_L to the time required to cross the eddy (Shirolkar et al., 1996; Mols and Oliemans, 1998). The following equations help in defining crossover time (t_c).

$$V_g = g\tau_p \tag{2.5a}$$

Equation 2.5a relates V_g, the drift velocity of the particle in the eddy, to the relaxation time of particle. The time required to crossover from one eddy to other eddy is given as follows:

$$t_c = \frac{L_e}{V_g} \tag{2.5b}$$

where L_e is the integral length scale of fluid and is assumed to be the length of the eddy. Cross trajectory effect is defined as the ratio of the lifetime of eddy, which is presumed to be the integral length scale of fluid, T_L, to the cross over time, t_c. Equation 2.5c defines cte

$$cte = \frac{T_L}{t_c} \tag{2.5c}$$

and after substituting for t_c from equation 2.5b, cte is as follows:

$$cte = \frac{g\tau_p T_L}{L_e} \tag{2.5d}$$

Reproduced with permission of the copyright owner. Further reproduction prohibited without permission.

In this work, as mentioned in the Section 4.1, slurries of particle size less than $250\mu m$ have been studied. Thus all the particles are smaller than η and can be referred to as small particles. Turbulent particle dispersion states according to Taylor theory of particle dispersion is a product of mean square fluctuating velocity of particle ($\overline{u_p'^2}$) and particle integral time scale (τ_{pL}). τ_{pL} is the particle analogue of T_L. Often particle dispersion is modeled with respect to the turbulent viscosity of the fluid (Mols and Oliemans, 1998; Shirolkar et al., 1996) as follows:

$$D_{tpd} \propto \nu_{tf} \times \mathrm{CTE} \times \mathrm{IE} \tag{2.6}$$

where D_{tpd} is the turbulent particle diffusivity, ν_{tf} is the turbulent viscosity of fluid and CTE and IE are cross trajectory and inertia effects, respectively, on particle turbulent diffusivity.

The effect of inertia on the particle dispersion is felt on both the factors influencing particle dispersion, τ_{pL} and $\overline{u_p'^2}$. By increasing inertia of a small particle (S< 1), $\overline{u_p'^2}$ decreases because of the reduction in fluctuations experienced on increasing inertia, but τ_{pL} increases, because on increasing inertia of the particle it becomes difficult to change particle velocity, hence particle velocity remains correlated for a longer time. Hence, it is difficult to predict the change in particle diffusivity due to inertia. However, in the current case, when the particle is small and $S < 1$, the effect of inertia has been modeled in the following way by Mols and Oliemans (1998).

$$\mathrm{IE} = \frac{1}{\sqrt{1+S}} \tag{2.7}$$

In Equation 2.7, on increasing inertia, S will increase, hence dispersion will decrease.

The effect of cross trajectory occurs in the presence of gravity. Cross trajectory effect does not affect $\overline{u_p'^2}$ (Mols and Oliemans, 1998; Shirolkar et al., 1996), it only affects τ_{pL}. This is because as discussed earlier, magnitude of velocity fluctuations experienced by a particle is directly related to inertia of the particle. By crossing over frequently from one eddy to another, the frequency of particle fluctuations increases but there is no change in the magnitude of the fluctuations. Thus, cross

Reproduced with permission of the copyright owner. Further reproduction prohibited without permission.

trajectory effect only reduces the time for which the particle velocity is correlated. Hence, particle diffusivity decreases in the presence of gravity (Mols and Oliemans, 1998). This effect has been modeled in the following way by Mols and Oliemans (1998):

$$\mathrm{CTE} = \frac{1}{\sqrt{1+\mathrm{cte}^2}} \tag{2.8}$$

in which, CTE is the effect of particles' tendency to cross over from one eddy to another on particle turbulent diffusivity. Thus, if a particle has a higher tendency to crossover from one eddy to another, cte increases according to Equation 2.5 and hence particle turbulent diffusivity decreases.

2.2.3 Turbulence Modulation

Eddies in turbulent flow disperse particles present in the flow. In turn, the addition of particles influences turbulence, which is termed as turbulence modulation. Thus, it is important to understand these effects to develop a two phase model. Tsuji et al. (1984) and Gore and Crowe (1989) have compiled various experimental results and reviewed the effect of particle size on turbulence modulation. Elghobhashi (1994) has studied the effect of volume fraction of solids. He finds that turbulence modulation starts after a volume fraction 10^{-6}, between 10^{-6} and 10^{-3} it is a two way coupling i.e. particles modulate turbulence and turbulence disperses the particles. Beyond 10^{-3} particle-particle interaction also become important.

The phenomena modulating turbulence as given by Lightstone and Hodgson (2004) are as follows:

- transfer of energy through drag force,
- interaction of particles with eddies, which breaks them into smaller eddies and causes dissipation,
- wake formation & vortex shedding
- and transfer of energy through cross trajectory effects.

The first two phenomena bring turbulence attenuation and the latter cause turbulence augmentation. Tsuji et al. (1984) and Gore and Crowe (1989) have concluded

Reproduced with permission of the copyright owner. Further reproduction prohibited without permission.

that augmentation of turbulence can occur only in the presence of large particles viz., when $d_p \geq 250\mu m$.

Most of the work to model turbulence modulation does not provide a general relation to model the change in eddy viscosity. Due to the use of more sophisticated turbulence models like k-ε, the above mentioned phenomena change equations for turbulent kinetic energy (k) and dissipation (ε). In turbulence modulation models, drag acts as the sink for turbulence kinetic energy (k) and wake formation and vortex shedding causes augmentation (Chen and Wood, 1985; Mostafa and Mongia, 1988; Yuan and Michaelides, 1992; Tu and Fletcher, 1994). Lightstone and Hodgson (2004) have added another term to account for production of turbulence due to cross trajectory effect.

Crowe et al. (1996) and Crowe (1999) have derived turbulent kinetic energy equation using a single phase mechanical energy equation and proposed the modulation to be proportional to a hybrid length scale for dense flows. Hybrid length scale is a function of the inter-particle spacing and dissipation length scale. The ratio of response time to integral time scale, loading ratio and ratio of particle diameter to turbulence length scale have been identified as important parameters to model turbulence modulation (Crowe et al., 1996). However, Roco and Shook (1985) and Hsu et al. (1989) have only incorporated the effect of turbulence dampening on eddy viscosity by using a concentration dependent function, to model slurry flows in pipelines.

2.2.4 Shear Induced Migration

The resuspension of a sediment layer in a fluid under laminar flow is called viscous resuspension. Leighton and Acrivos (1985, 1987a,b) have attributed viscous resuspension to shear induced diffusion i.e., drift of particles from high to low shear stress region due to particle-particle interaction in a shear flow. This led to a series of research on viscous resuspension in Poiseuille flow (Schaflinger et al., 1990; Philips et al., 1991; Zhang and Acrivos, 1994) and Couette flow (Acrivos et al., 1993).

Reproduced with permission of the copyright owner. Further reproduction prohibited without permission.

Leighton and Acrivos (1987a,b) have measured shear induced diffusion coefficients and have explained these observations using irreversible interparticle interactions. Consider a shear flow of varying concentration suspension, with shear rate as Υ, in-situ concentration as Φ and concentration and Υ vary in y-direction. During interparticle interactions, particles collide with another particle at a rate proportional to $\Upsilon\Phi$. Displacements experienced by a particle during these collisions are proportional to particle diameter, d_p. They have recognized three important gradients which lead to particle drift in a shear flow i.e. concentration, viscosity and shear rate. In the presence of any of these gradients, a gradient is induced either in the rate of interactions ($\propto \Upsilon\Phi$) or in the order of displacement ($\propto d_p$). These mechanisms have been well explained in Leighton and Acrivos (1987b) and Philips et al. (1991) as follows:

Concentration Gradient: Due to a concentration gradient, a particle will experience more interactions at the higher concentration side, thus a particle will drift from high to lower concentration. The excess rate of interactions is $\propto (\Upsilon d_p)(d\Phi/dy)$. The flux due to this drift is $\propto (\Upsilon\Phi d_p^2)(d\Phi/dy)$

Viscosity Gradient: Due to viscosity gradient a particle experiences more resistance to its displacement in high viscosity region hence the particle migrates from high to low viscosity region. Displacement is scaled as $\propto (d_p/\mu)(d\mu/dy)$ The flux due to this phenomenon is $\propto \Upsilon d_p^2(\Phi^2/\mu)(d\mu/d\Phi)(d\Phi/dy)$. Viscosity gradient is a strong function of concentration gradient, hence this diffusion is stronger than due to only concentration gradient alone.

Shear Rate: Due to shear rate gradient a particle will experience more collisions in high shear rate region, hence the particle will drift away to low shear region. The rate of interaction is $\propto (\Phi d_p)(d\Upsilon/dy)$ and flux is $\propto (\Phi^2 d_p^2)(d\Upsilon/dy)$

Philips et al. (1991) have extended the concept of shear induced migration to Poiseuille and Couette flows. Shear induced flux expressions were based on scaling arguments derived by Leighton and Acrivos (1987a). The model results agree well with the experimental results for different particle sizes.

Reproduced with permission of the copyright owner. Further reproduction prohibited without permission.

Zhang and Acrivos (1994) have solved a fully developed flow in horizontal pipe for nearly neutrally buoyant particles. They did a 2-D analysis on the cross-section in fully developed region and incorporated secondary flow also. Though it is small compared to the axial flow, it arises due to the concentration gradient and also contributes in suspending the particles in the flow.

Reproduced with permission of the copyright owner. Further reproduction prohibited without permission.

Chapter 3

Experimental Setup and Testing of The Piston Sampler

3.1 Experimental Setup

A schematic diagram of the experimental loop used by Razzaque et al. (2003) to conduct air-water flows is shown in Figure 3.1. In this study too, experiments were carried out only for air-water flows. The 35 m long horizontal loop is made of 25.4 mm ID copper tube. A 2.24 kW (3HP) progressive cavity pump [Moyno pump] (P) driven by a variable speed motor is used to circulate water in the loop at a velocity of up to 2.9 m/s. A coriolis mass flow meter [Krohne MFM 4085K Corimass, type 300G+] (F) is used to measure mass flow rate, volumetric flow rate and temperature of the flow. A 4 m long double pipe heat exchanger (H) is used to keep the temperature of the loop steady at 17 ± 1.0°C. The only source of heat generation in the flow is the wall-friction due to the flowing water. This small amount of heat was removed by flowing cold water in the outer pipe when the temperature inside the inner pipe exceeded 18.0°C. The flow of cold water was stopped as soon as the temperature reached 16.0°C. Three viewing sections (V1, V2 and V3) made of 25.4mm ID glass tube were placed in the loop. A glass box of rectangular cross-section was fitted over each glass tube. The space between the rectangular box and the tube was filled with silicone oil and thus the curvature effect of the tube was removed and undistorted images of bubbles could be obtained. Silicone oil was used to fill the gap because refractive index of water and silicone oil is very similar which helps in removing the curvature effects. Bubble size distributions can

Reproduced with permission of the copyright owner. Further reproduction prohibited without permission.

be measured at all three viewing sections V1, V2 and V3 when air was injected through injector A1. V1, V2 and V3 are located 0.3, 15 and 27.5 m downstream of the injector A1, respectively. Compressed air was continuously injected through a

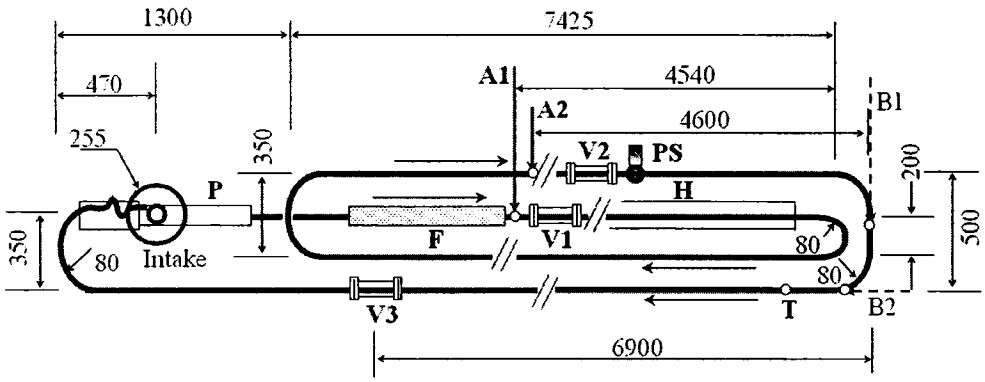

(a) Partial Plan View

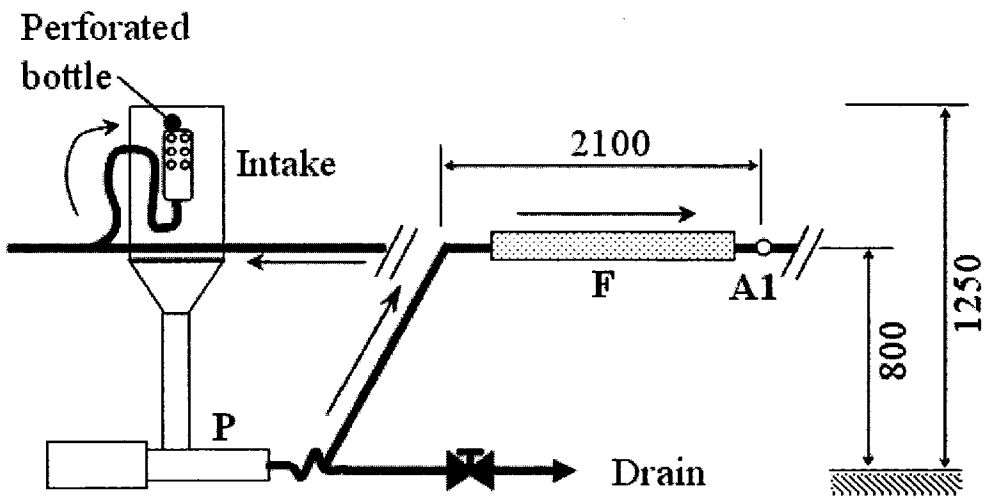

(b) Partial Front View

Figure 3.1: Schematic diagram of the experimental loop. P- Moyno pump, F - Coriolis flow meter, H - Heat Exchanger, T - Thermocouple, A1, A2, B1 and B2 - Air injection points, V1, V2, V3 - Viewing sections, PS - Piston Sampler. Arrows indicate flow direction. Dimensions are in mm.

2 or 4mm ID stainless steel tube, which formed a simple T-junction with the loop. The air flowrate was measured with an Air Flow Meter (Omega FMA 5400-5500), placed in the air supply line. The cross-sectional area of the tank at the inlet of the pump was made large enough to let the air bubbles escape easily to atmosphere.

Reproduced with permission of the copyright owner. Further reproduction prohibited without permission.

Figure 3.2: Photograph of the viewing section as installed on the pipeline

The air–water mixture is discharged tangentially at a height of 1100mm from the ground into the tank. It makes the flow into the coriolis mass flow meter free from air bubbles as the air injection points are located further downstream. The average water velocity, can be determined from the recorded volumetric flow rate by dividing it with the pipe cross-sectional area.

3.1.1 Photographic Technique

A high speed camera connected to a computer was used (PCI Motionscope 1000S) to record bubbles passing through the viewing sections. It can record at a rate of 1000 frames per second (fps) and can store 1024 frames in memory. In the present study, while photographing at viewing section V2, as shown in Figure 3.2, an imaging rate of 500fps was used to provide a larger resolution. The recorded video and frames were saved in AVI and JPEG formats respectively. The photos from the camera are gray scale images. All the frames were converted into Black and White images using MATLAB Image Processing Toolbox. The MATLAB processed image has black a background with white bubbles, as shown in Figure 3.3. The Matlab code labels all the bubbles and provides the area of each bubble. The bubble size is determined from the projected area of the bubble as follows:

$$d_b = \sqrt{\frac{4A}{\pi}} \tag{3.1}$$

For each run, more than 300 bubbles were scanned to determine the bubble size distribution. This method imposes two limitations on the flow conditions:

Reproduced with permission of the copyright owner. Further reproduction prohibited without permission.

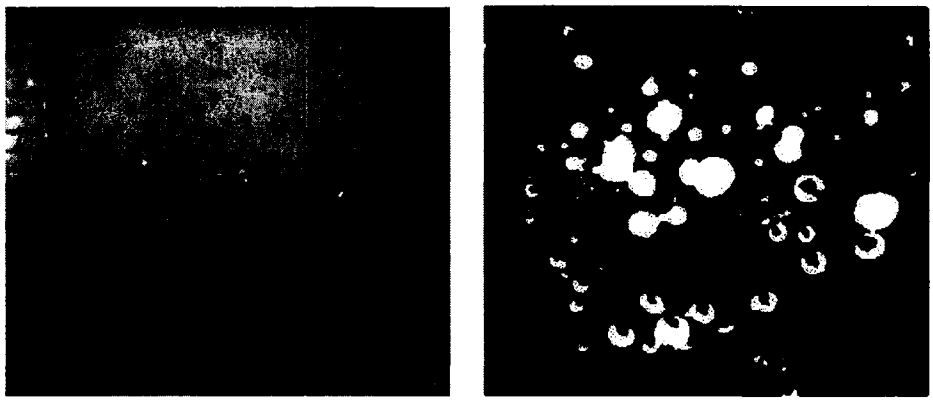

(a) Sample grayscale image from viewing section

(b) MATLAB processed image

Figure 3.3: Sample grayscale image taken from top of viewing section and corresponding MATLAB processed image

1. The bubble size is determined from their projected area, thus it is assumed that bubbles are spherical. For the bubbles to be spherical, the flow should be highly turbulent. Thus, experiments should be conducted at high water flow rates.

2. As the air volume fraction increases, bubble size and number increases. As a result, increasing number of bubbles appear joined in the images. Since an edge detection technique is used to locate the bubble, it becomes increasingly difficult to distinctly identify a bubble. In a MATLAB processed image big white blobs are observed in most of the frames which forces us to omit a large fraction of bubbles, which leads to an erroneous measurement of BSD. The MATLAB code is listed in Appendix A.

3.1.2 Piston Sampler

The piston sampler has been designed in such a way that it will grab a 2ml sample from the pipeline and release the sample to a column of water, through which bubbles will rise and sand particles will settle down. A schematic of the piston sampler is shown in Figure 3.4. It also shows the dimensions of plunger when it rests inside the pipeline, and when it comes out of the pipeline thereby

Reproduced with permission of the copyright owner. Further reproduction prohibited without permission.

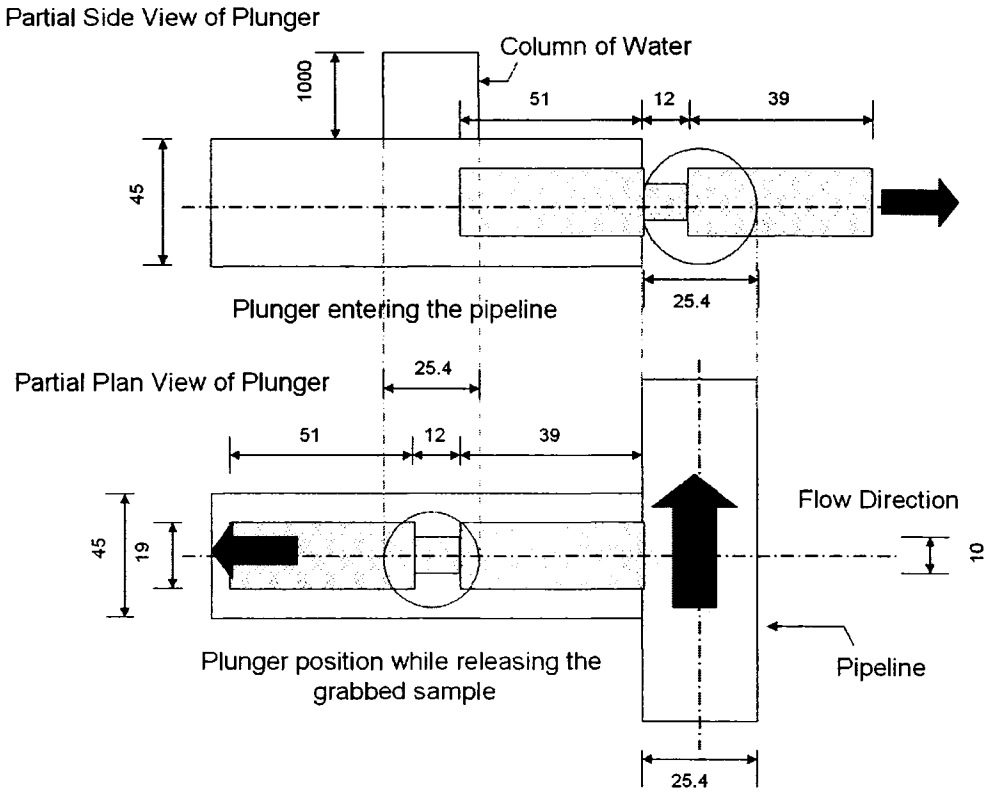

Figure 3.4: The Piston Sampler. Arrows indicate direction of flow and piston motion. Dimensions are in mm.

releasing the sample. Figure 3.5b shows the sampler installed on the pipeline with a column of water above it. The sampler has a two way switch which operates on compressed air. One switch triggers the plunger into the pipeline, across the flow direction and along the horizontal axis of the pipeline cross-section as shown in Figure 3.4. The other switch will bring plunger out from the pipeline along with the sample. Figure 3.5a shows the piston sampler from the top, with the plunger outside sampler. After grabbing the sample from the pipeline, bubbles are released into the water column from the opening that can be seen in Figure 3.5a.

The design of the piston sampler poses two limitations as follows:

1. The plunger in its current position grabs the sample along the central horizontal axis of the pipeline cross-section, whereas most of the air bubbles are at the top. Hence, there is a possibility that the grabbed sample might not be

Reproduced with permission of the copyright owner. Further reproduction prohibited without permission.

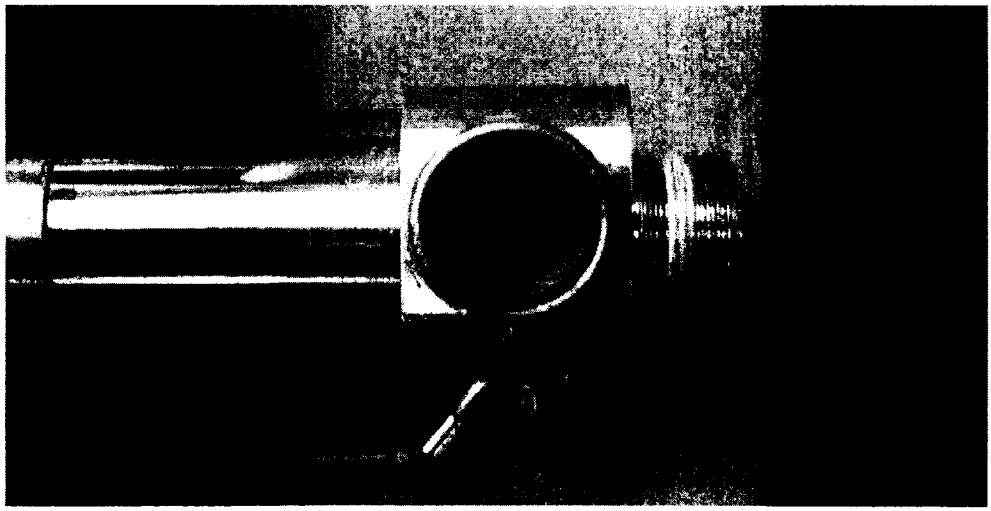

(a) Top View of Piston Sampler

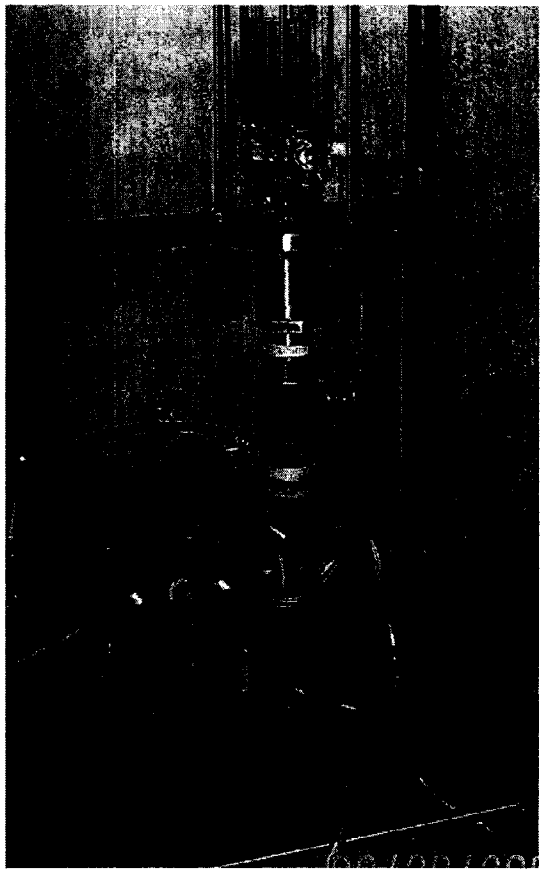

(b) Piston Sampler installed on the pipeline

Figure 3.5: Photographs of The Piston Sampler

Reproduced with permission of the copyright owner. Further reproduction prohibited without permission.

representative of all the bubbles in the pipeline.

2. While grabbing the sample, plunger interferes with the flow; thus it is very likely that bubbles will be broken during the process.

The experiments have been designed to reduce the effect of the above mentioned limitations resulting from the design of plunger and the photographic technique and to test the plunger as BSD measurement technique. To ensure that both the imaging technique and plunger are measuring the same BSD, the piston sampler was installed in close proximity to the viewing section V2, and since the plunger intrudes in the pipeline it was installed downstream of the viewing section as shown in Figure 3.1 labelled 'PS'.

While recording bubbles rising through the column of water, a recording rate of 60fps was used to record for a longer time i.e. 8 seconds. The recorded frames were analysed in the same way as above, i.e. using MATLAB Image Processing Toolbox. Again, bubble sizes were determined from the projected area. The number of bubbles in each video varied from 6-20. At least 300 bubbles have been scanned to determine the BSD, thus approximately 30 videos were taken for each run. The bubbles in the column of water are spherical in shape and the over crowding of bubbles is not observed in this measurement.

3.1.3 Operation of Pipeline Loop and Piston Sampler

The following steps were performed to operate the pipeline loop and the camera.

1. Water was supplied to the stand tank and pipeline. Power was provided to the motor once the loop and stand tank were full. The pump was slowly increased to 500RPM with the water supply still continuing as the pipeline still has some air in it. Water supply is stopped once the stand tank fills to the maximum level, above which water is splashed around at high flow rates (approximately after 1300RPM).

2. Coriolis mass flow meter was started and the flow rate was set to desired level by changing the pump RPM. Air flow to the air flow meter was then started,

Reproduced with permission of the copyright owner. Further reproduction prohibited without permission.

followed by air flow inlet to the pipeline. This step was followed to avoid back flow of water into the air flow meter. The air flow meter was set to desired level and the system was allowed to achieve steady state by waiting for 5 minutes.

3. The temperature of the flow was closely monitored to maintain it at $17\pm1°C$ by controlling the supply of cold water.

4. The lights and camera were then installed on viewing section V2 to take videos from the top. At this moment it was ensured that plunger was outside the pipeline.

5. After the system has achieved steady state 3 videos were taken from the top. The videos were saved as .AVI file and frames were saved as .JPEG images. The air and water flow rates were changed to desired levels. Without disturbing the position of camera and lights, 3 videos were shot for every different combination of air−water flows.

6. The air flow to the pipeline was stopped to take background video without any bubbles. The system was allowed to run for 5 minutes to remove the air from the pipeline. A small video was taken without disturbing the lights and camera. The video was not saved but frames are saved as .JPEG images.

7. Air flow rate was again started and was set at a desired rate. Camera and lights were installed on the water column above piston sampler. The plunger was triggered inside the pipeline and the system was allowed to achieve steady state.

8. Piston sampler was triggered out of the pipeline and then brought back inside the pipeline. Meanwhile the small sample from pipeline was grabbed and released to the water column. The camera was started and stopped approximately after 12 seconds. Videos were not saved and frames were saved as .JPEG images. A separate background video was not taken, as there are very few bubbles in this video, thus there are lots of frames without any bubbles in it. This process was repeated 30 times.

Reproduced with permission of the copyright owner. Further reproduction prohibited without permission.

9. After the runs were completed, the air supply to pipeline was stopped, followed by air flow meter, main air supply and coriolis flow meter. The RPM of pump was reduced to zero, followed by shutting down of the power to motor. The pipeline water was discharged by opening the exit valve.

3.1.4 Matlab Image Processing

Frames saved from videos of high speed camera were gray scale images. All the images included a scale to calibrate the pixel size. A background image without any bubbles in it is also used for image processing. The following procedure is used to measure BSD with MATLAB for a given air−water flow rate.

1. The grayscale image of bubbles was converted into a black and white image, with bubbles as white and background as black using a series of MATLAB commands given in appendix A. A brief overview of the procedure is as follows:

   - The background of the grayscale image is removed to have an image only with the bubbles.
   - A threshold grayscale level was chosen as basis to convert the image into a black and white image.
   - Bubbles, termed as 'holes' in MATLAB, were filled to complete the bubbles whose edges have been detected.

2. Every separate 'white' spot was then labeled using MATLAB. Labeling of the spots starts from top left to right and then goes till the bottom of the image. The labeling area of each spot was saved along with the labeled black and white image.

3. The above algorithm is followed for all the frames in all the videos.

4. The saved image was then opened using another series of MATLAB commands, which are given in Appendix A. The areas of the 30 largest bubbles are printed beside the bubbles.

Reproduced with permission of the copyright owner. Further reproduction prohibited without permission.

5. One of the grayscale image was used to measure the pixel size. The area of bubbles was then converted from pixel size into diameter in mm using the calibration scale and Equation 3.1.

6. The steps from 4-6 were repeated until 300 bubbles were scanned.

3.2 Experimental Runs

3.2.1 Limitations in Comparison

Since the two techniques have to be compared to check the piston sampler as a BSD measurement technique, pipeline conditions should be such that they do not fall outside the known limitations of the set-up. As already discussed, the imaging technique on viewing section V2 fails at higher air fractions. With the piston sampler, the small sample grabbed from the pipeline at low air fractions is not representative of pipeline conditions because the number of bubbles present in the small sample varies from none to three. Thus, the two measuring techniques pose opposing limitations on air flow rates.

Most of the runs were conducted at highest water flow rate allowed by the pump. Due to the wearing of the pump over the years, maximum water velocity has decreased from 2.9 m/s to 2.2 m/s. In the previous studies conducted by Razzaque et al. (2003), a water velocity of 2.9 m/s and volume fraction of 0.0015 were found to lie in the coalescence dominant regime. Thus, to maintain the sphericity of the bubbles, it is important to operate at the maximum capacity of the pump. The variation in BSD can be obtained either by varying the flow rate or air volume fraction. The results from the previous study (Razzaque et al., 2003) have shown that BSD is more sensitive to water flow rate than air volume fraction. In this study, the air fraction was chosen at 0.5%. Above that volume fraction of air, videos from the viewing section V2 can give erroneous BSD's. The lowest flow rate for the runs was limited by the following conditions. The greater of the two was chosen as lowest velocity.

1. The flow rate at which bubbles deform and are no longer spherical in shape.

Reproduced with permission of the copyright owner. Further reproduction prohibited without permission.

2. The flow rate at which the sample grabbed by piston sampler contains less than 6 bubbles on an average.

Four runs were conducted, three of them at air fraction of 0.005 and velocities as 2.2 m/s, 1.9 m/s and 1.6 m/s and the fourth at air fraction of 0.0022 and velocity as 2.2 m/s. The temperature was maintained at 17±1°C for all the experiments.

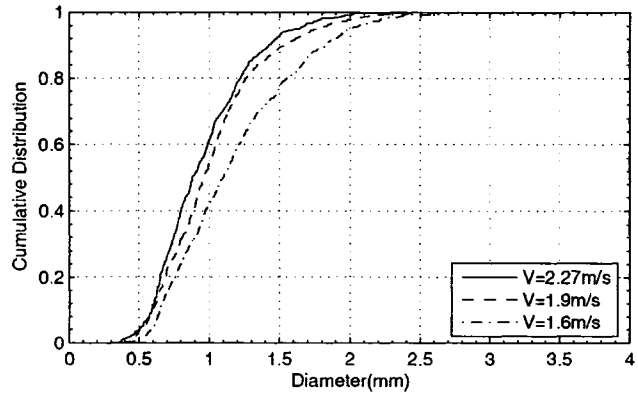

Figure 3.6: Effect of flow rate on BSD as measured with the photographic technique. Air Fraction = 0.005

3.2.2 Experimental Results

The experimental results of both photographic and piston sampler, were compared to study the accuracy of piston sampler. Figure 3.6 shows cumulative BSD for varying flow rate as measured from viewing section. The results were as expected. As the velocity decreases, the turbulence level in the pipeline goes down thereby increasing the average bubble size. Thus, as velocity goes down, cumulative BSD's shift towards right. Figure 3.7 also compares cumulative BSD's from piston sampler for varying flow rates. The plot does not follow the intuitive behavior. It gives identical cumulative BSD curves for all the flow rates.

When cumulative BSD's from viewing section and piston sampler are compared, it can be seen that the difference between the measurements widens as the water flow rate decreases. Figure 3.8 compares cumulative BSD's from viewing section and piston sampler at different air volume fractions. The same trend is observed, where cumulative BSD's do not change and the results from viewing section

Reproduced with permission of the copyright owner. Further reproduction prohibited without permission.

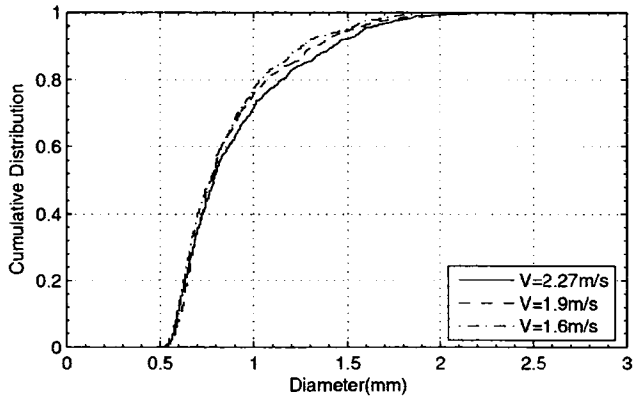

Figure 3.7: Effect of flow rate on BSD measured with the piston sampler. Air fraction = 0.005

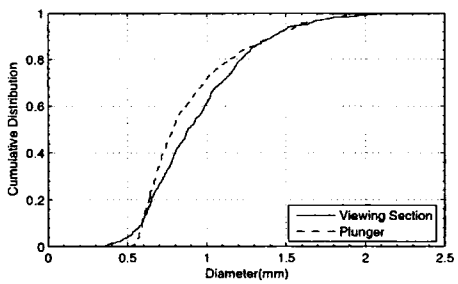

(a) BSD for Air Fraction = 0.005 and Flow Rate = 2.2m/s

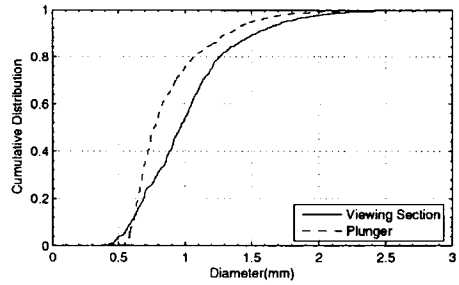

(b) BSD for Air Fraction = 0.005 and Flow Rate = 1.9m/s

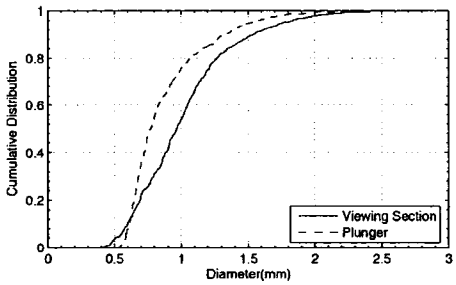

(c) BSD for Air Fraction = 0.005 and Flow Rate = 1.6m/s

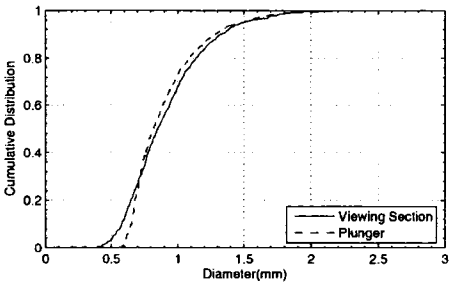

(d) BSD for Air Fraction = 0.0022 and Flow Rate = 2.2m/s

Figure 3.8: Comparison of BSD from piston sampler and photographic technique

follow the theory, viz. on increasing the air fraction larger bubbles were observed and hence cumulative BSD shifts to the right. Thus the following conclusions can be drawn about the performance of the piston sampler during the tests:

1. Currently, the plunger captures the sample from the centre of the pipeline and

Reproduced with permission of the copyright owner. Further reproduction prohibited without permission.

the variation in air fraction and velocity is insufficient to significantly change the BSD. Thus, it is possible that plunger is giving the air BSD at centre of pipeline, which is not changing significantly with the varying velocity and air fraction.

2. Since the average bubble size measured with the piston sampler is smaller than that obtained from the photographic technique, the piston might be breaking the bubbles.

The BSD at the current position from where plunger grabs the sample is not changing significantly. Thus, before concluding anything with the piston sampler, more experiments have to be conducted at higher flow rates or the vertical position of the piston entry should be changed.

Reproduced with permission of the copyright owner. Further reproduction prohibited without permission.

Chapter 4

Slurry Flow Model

4.1 Formulation of Slurry Flow Model

The current study has used a single fluid model to model slurry flows in pipelines. As mentioned in Section 2.2, modeling particle dispersion has been critical to slurry flow modeling. The particle dispersion model of Roco and Shook (1983) balanced gravitational force with turbulent and particle-particle interaction dispersive forces. Granular temperature (particle-particle interaction flux arising in turbulent flows due to fluctuations experienced by particles) modeling involves a lot of empirical constants. Hence, an attempt has been made to model granular temperature, by developing a model for a flow regime where gravitational flux is largely balanced by granular temperature and turbulent dispersion. In the current study, the model has been developed for regimes where the flow velocity is above the deposition velocity. Thus, turbulence is high enough to disperse the particles and hence, Bagnold and Coulombic forces have been neglected. The particle sizes are small, $d_p < 250\mu m$ and hence lift force due to slip between particles and fluid can be neglected. Both granular temperature and turbulent dispersion have been modeled by incorporating turbulence in a macroscopic way. Momentum balance has also been modeled by including turbulence in a macroscopic sense by introducing the turbulent viscosity of slurry. This way of modeling slurry flows is unique and has not been done before.

The following assumptions were made to model slurry flows using Eulerian approach :

- The flow was assumed to be fully developed and at steady state. By assuming

Reproduced with permission of the copyright owner. Further reproduction prohibited without permission.

fully developed flow, it is reasonable to neglect variation in the axial direction of the pipeline.

- Mean particle size in the slurry is less than $250\mu m$.

- Flow velocities were assumed to be higher than the deposition velocity. Thus, slip velocity between the particle and liquid was assumed to be negligible, hence a single momentum equation for slurry phase was solved along with a convection-diffusion transport equation for particles. The effect of lift force was neglected as particles are smaller than $250\mu m$.

- Turbulence was assumed to be HIST. An important quantity derived from turbulence modeling, directly influencing momentum equation, is turbulence viscosity. Several closure models exist for turbulent viscosity. Prandtl Mixing Length proposes a relation proportional to shear rate. More sophisticated models introduce variables like turbulent kinetic energy (k) and dissipation (ε) and explicitly relate turbulent viscosity with these variables. A commonly used model is the two equation k-ε model which solves a convection-diffusion kind of equation for turbulent kinetic energy and dissipation. In this study, turbulent viscosity was assumed to be independent of in-situ velocity and shear rate, though it is assumed to be a function of concentration, which is discussed later in Section 4.1.1. Thus, the momentum equation for the axial velocity is similar to laminar flow of a highly viscous fluid.

By assuming fully developed flow, variations in axial direction were neglected and hence momentum and mass transport equations were applied to the 2-D cross-section of the pipeline. Figure 4.1 shows the co-ordinate system and 2-D cross-section of the pipeline. Gravity acts in the negative x_2-direction and flow is in the x_3-direction. Turbulent flow equations developed for slurry flows are dimensionless and are an extension of the equations used by Zhang and Acrivos (1994) for laminar flows. The equations are as follows:

$$\frac{\partial u_j}{\partial x_j} = 0, \tag{4.1a}$$

Reproduced with permission of the copyright owner. Further reproduction prohibited without permission.

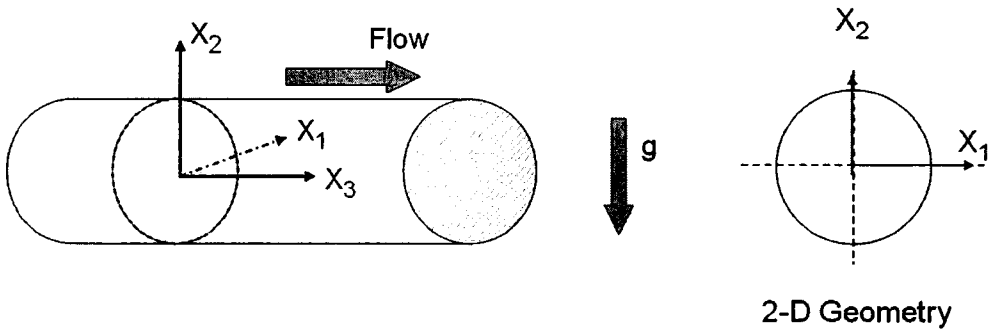

Figure 4.1: Flow Domain and Co-ordinate System

$$Re(1+\rho_d\Phi)(\frac{\partial u_i}{\partial t}+u_j\frac{\partial u_i}{\partial x_j}) = \frac{\partial}{\partial x_j}[-p\delta_{ij}+2\nu_{ts}(\Phi)\dot{\gamma}_{ij}]-\frac{1}{Fr}\Phi\delta_{2j},\ \text{i=1,2} \quad (4.1b)$$

$$Re(1+\rho_d\Phi)(\frac{\partial u_i}{\partial t}+u_j\frac{\partial u_i}{\partial x_j}) = K+\frac{\partial}{\partial x_j}(2\nu_{ts}(\Phi)\dot{\gamma}_{ij}),\ \text{i=3} \quad (4.1c)$$

where Re is given by,

$$Re = \frac{\rho_f UL}{\mu_f} \quad (4.1d)$$

where Fr is modified Froude number given by,

$$Fr = \frac{\mu_f U}{(\rho_p-\rho_f)gL^2} \quad (4.1e)$$

where $\dot{\gamma}$ is given by

$$\dot{\gamma} \equiv \frac{1}{2}(\nabla u+\nabla u^T) \quad (4.1f)$$

where ρ_d is given by

$$\rho_d = \frac{\rho_p-\rho_f}{\rho_f} \quad (4.1g)$$

and K is the dimensionless pressure drop. The pressure drop is unique to every mean flow rate Q, but there is no explicit equation relating K and Q. However, Q is directly dependent on the axial velocity and K is solved using the flow rate equation as follows:

$$Q = \int_\Omega u_3 d\Omega = \frac{\pi}{2} \quad (4.1h)$$

Characteristic length (L) and velocity (U) of the flow are radius of pipe and mean flow rate(U_{avg}) of slurry, respectively. $\nu_{ts}(\Phi)$ is dimensionless turbulent viscosity of slurry, which shall be discussed in detail in Section 4.1.1. The pressure in the

Reproduced with permission of the copyright owner. Further reproduction prohibited without permission.

momentum balance for x_1 and x_2-direction, p, is defined using penalty formulation as follows:

$$p = -\alpha \mathrm{Re} \nu_{ts}(\Phi) \frac{\partial u_j}{\partial x_j} \tag{4.1i}$$

where α is the penalty parameter chosen to be a very high value. In the current study α is chosen to be 1000. The boundary for the flow is wall where no slip condition is assumed. This forms the boundary conditions for the momentum equations. This set of equations 4.1 requires appropriate models for bulk properties like density and turbulent viscosity of slurry (ν_{ts}).

4.1.1 Turbulent Viscosity of Slurry

There are no empirical or phenomenological expressions available for this concept. It can be explained as the turbulent analogue of slurry shear viscosity. Figure 4.2 explains the analogy between shear viscosity and turbulent viscosity of slurry. In a shear flow of a Newtonian fluid, stress is related to strain by a proportionality constant called shear viscosity. Addition of particles to fluid changes its viscosity. The mixture viscosity has been measured and several empirical relations exist relating the mixture viscosity to the particle density, volume fraction and diameter. These correlations have been reviewed in Shook and Roco (1991). Similar to shear flow, in turbulent flow of a Newtonian fluid stress is related to strain by a proportionality constant called turbulent viscosity. On addition of particles to the fluid, the turbulent viscosity of the mixture has been termed as turbulent viscosity of slurry. Turbulent viscosity of mixture has been modeled in three steps. It can be divided

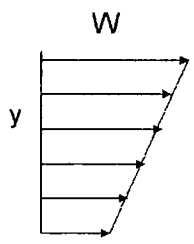

	Laminar Flow	Turbulent Flow	Laminar Flow with Particles	Turbulent Flow with Particles
Shear Stress	$\mu \frac{dW}{dy}$	$\mu_t \frac{dW}{dy}$	$\mu(\phi) \frac{dW}{dy}$	$\mu_t(\phi) \frac{dW}{dy}$

Figure 4.2: Analogy between Shear and Turbulent Viscosity of Slurry

into three independent phenomena.

Reproduced with permission of the copyright owner. Further reproduction prohibited without permission.

- The turbulent viscosity of liquid phase.
- As particles are added the turbulence level in carrier phase changes which is referred to as turbulence modulation. This change can result in increased and decreased turbulence levels.
- Similar to the shear viscosity, turbulence viscosity of mixture depends on the shape and concentration of particle.

The final expression for turbulent viscosity is as follows:

$$\begin{aligned} \text{Slurry Turbulent Viscosity} &= \text{Turbulent Viscosity Of Carrier Fluid} \\ &\times \text{Turbulence Modulation} \\ &\times \text{Particle Characteristics} \end{aligned} \tag{4.2a}$$

$$\nu_{ts} = \nu_{tf} \times \nu_{tm} \times \nu_{tp} \tag{4.2b}$$

Turbulent Viscosity of Carrier Fluid

Friction factor for a single phase turbulent flow in pipeline implicitly depends on Reynolds number. The colebrook relation for friction factor has been used to obtain an empirical relation for turbulent viscosity of carrier phase with Reynolds number. The following algorithm has been used to find turbulent viscosity of carrier phase.

1. For any given Reynolds number, friction factor was calculated using the colebrook equation.
2. Using the friction factor, pressure drop for the Reynolds number was calculated.
3. Single phase hydrodynamic equations were solved for turbulent viscosity of carrier fluid using the developed model in the absence of particles, and pressure drop calculated in Step 1.

Reproduced with permission of the copyright owner. Further reproduction prohibited without permission.

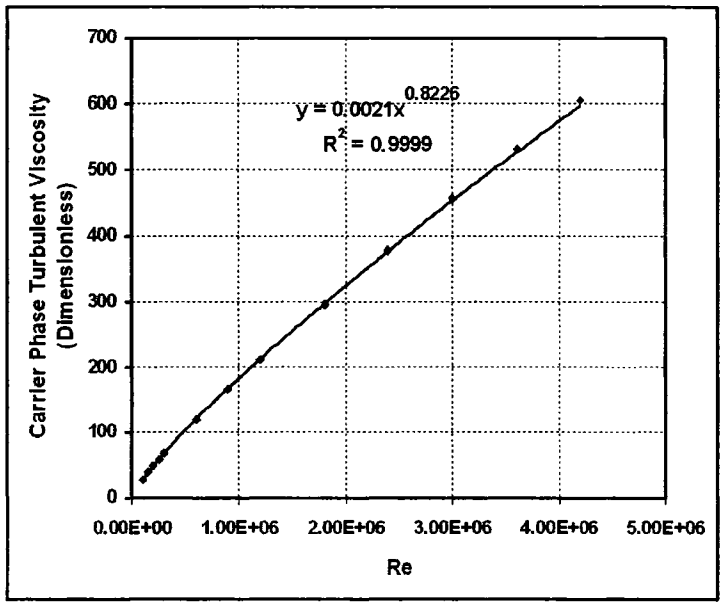

Figure 4.3: Dimensionless Turbulent Viscosity of Carrier Phase vs. Reynolds Number

4. Steps 1-3 were repeated for eight different Reynolds numbers, which was varied by changing flow velocity and pipeline diameter. The Polyfit function in Excel was used to fit turbulent viscosity of single phase with Reynolds number.

Figure 4.3 shows carrier phase turbulent viscosity calculated using the developed model with Reynolds number.

$$\nu_{tf} = b_{10}\mathrm{Re}^{0.8226} \tag{4.3}$$

The curve fit shows that ν_{tf} is $\propto Re^{0.8226}$. This power law relationship between turbulent viscosity and Reynolds number agrees well with Walton (1995).

Turbulence Modulation

As particles are added to the carrier phase, the turbulence level changes depending on the particle size and concentration. Lightstone and Hodgson (2004) state that turbulence augmentation occurs for particles greater than 250μm. Here, slurries have been assumed to consist of particles $\leq 250\mu m$, thus it can be safely assumed that turbulence is dampened on addition of particles. As mentioned earlier, there is

Reproduced with permission of the copyright owner. Further reproduction prohibited without permission.

no general equation in the literature to model the change in turbulent viscosity of carrier phase. However, Roco and Shook (1985) and Hsu et al. (1989) have used equation 4.4, to account for turbulence modulation on turbulence viscosity.

$$\nu_{tm} = 1 - \frac{\Phi_p}{\Phi_m} \tag{4.4}$$

Here turbulence modulation is proposed to be modeled in the following way in this study:

$$\nu_{tm} = e^{-\Phi_p/\Phi_m} \tag{4.5}$$

At high concentration of particles, turbulence might be dampened significantly that it could lead to a laminar flow Bagnold (1956), and thus Equation 4.4 physically makes sense, because at high concentrations turbulence viscosity approaches zero and shear viscosity will become dominant. But under the current study shear viscosity has been completely neglected hence Equation 4.5 has been chosen over equation 4.4.

Particle Concentration and Shape Effect

By adding particles there is a two way effect: turbulence modulation as discussed above, and the increase in turbulent viscosity of the slurry due to the presence of particles. This effect is modeled in the same way as it is done for shear viscosity. The following expression is proposed to model particle characteristics i.e shape and concentration:

$$\nu_{tp} = 1 + b_1\Phi^{b_2} + \frac{b_3}{((\Phi_m/\Phi)^{1/3} - 1)^2} + b_4\frac{d\Phi}{dx_2} \tag{4.6}$$

where $b_2 \leq 1$. The third term in the right hand side of Equation 4.6 incorporates the effect of particle concentration. It is similar to the shear viscosity modeling used by Schaan et al. (2000). The shape of every type of particle has been characterised by a maximum packing fraction. The last term in equation 4.6 is the gradient of concentration in the direction of gravity. This term makes turbulent viscosity sensitive to changes in concentration.

Reproduced with permission of the copyright owner. Further reproduction prohibited without permission.

4.1.2 Scalar Transport of Particles

Transport of particles is modeled using a convection-diffusion kind of equation. Since there is no secondary flow, convection is almost negligible in the cross plane perpendicular to the flow direction. Diffusional flux consists of three main components: Gravitational Flux, Turbulent Dispersion Flux and Particle-Particle Interaction Flux. Gravitational flux tries to settle the particles, but particles are suspended by turbulent dispersion and particle-particle interaction flux, which are a result of particle interaction with eddies and with other particles themselves respectively.

The equations for particle transport have been developed for 2-D, a steady state is assumed, and secondary flow is not neglected. The convection-diffusion equation for particles is as follows:

$$\begin{aligned} u_1\frac{\partial\Phi}{\partial x_1} + u_2\frac{\partial\Phi}{\partial x_2} &= \text{Gravitational Flux} \\ &+ \text{Turbulent Dispersion Flux} \\ &+ \text{Particle-Particle Interaction Flux} \end{aligned} \tag{4.7a}$$

or

$$u_1\frac{\partial\Phi}{\partial x_1} + u_2\frac{\partial\Phi}{\partial x_2} = \frac{\partial\Phi}{\partial x_1}[D_{tpx1}\frac{\partial\Phi}{\partial x_1}] + \frac{\partial\Phi}{\partial x_2}[D_{tpx2}\frac{\partial\Phi}{\partial x_2} + N_G] \tag{4.7b}$$

Boundary conditions consist of a no flux condition as no material leaves the pipeline. But no flux condition on all boundaries does not define the system completely. Information on average concentration in the following form is used as the boundary condition and to define the system completely.

$$\frac{\int_\Omega \Phi d\Omega}{\int_\Omega d\Omega} = \Phi_p \tag{4.8}$$

Gravitational Flux

Due to the presence of gravity particles tend to settle; this kind of particle transport is called gravitational flux and is based on the settling velocity of particles. Settling velocity is calculated for Stokes' regime. An approach similar to Zhang and Acrivos (1994) has been used to arrive at the following expression for gravitational flux:

$$N_G = \frac{2}{9}(\frac{d_p}{L})^2\frac{1}{Fr}\Phi f(\Phi) \tag{4.9}$$

Reproduced with permission of the copyright owner. Further reproduction prohibited without permission.

where f is the correction factor for hindrance due to the presence of many particles

$$f = \frac{1-\Phi}{\mu_r} \tag{4.10}$$

and μ_r is

$$\mu_r = (1+\frac{1.5\Phi}{1-\frac{\Phi}{\Phi_m}})^2 \tag{4.11}$$

Turbulent Dispersion Flux and Particle-Particle Interaction Flux

Turbulent dispersion flux arises due to the interaction of particles with eddies. Thus, if a particle did not have inertia, particle diffusivity will be similar to eddy diffusivity. But due to particle's inertia and presence of gravity, two factors play a role to determine the final diffusivity i.e. Inertia Effect (IE) and Cross Trajectory Effect (CTE). In the current study, L_e has been assumed as one tenth of pipe diameter and T_L is assumed as ratio of D_t and U_{avg}, similar to Mols and Oliemans (1998). Since gravity acts only in x_2-direction, hence cross trajectory effect on diffusivity is incorporated only in x_2-direction. These phenomena are modeled in the same way as done by Mols and Oliemans (1998) and has been explained in section 2.2.2:

$$\text{IE} = \frac{1}{\sqrt{1+\frac{\tau_p}{T_L}}} \tag{4.12a}$$

$$\text{CTE} = \frac{1}{\sqrt{1+(\frac{10g\tau_p T_L}{D_t})^2}} \tag{4.12b}$$

Since turbulence is modulated upon the addition of particles, thus turbulent diffusivity is also modulated. Dampening factor (D_{damp}) is used to model turbulence modulation, in the absence of particles D_{damp} will be unity and as Φ_p increases D_{damp} approaches a constant value. D_{damp} is proposed to be modeled as follows:

$$D_{damp} = b_6 \times e^{-\Phi/\Phi_m} \tag{4.13}$$

The turbulence dampening function is inadequate for high concentrations, as dampening occurs more rapidly and can also lead to a laminar flow, Bagnold (1956). As mentioned earlier in section 2.2.2, particle diffusivity is proportional to turbulent

Reproduced with permission of the copyright owner. Further reproduction prohibited without permission.

viscosity of fluid, ν_{tf}, which itself is dependent on Re, as mentioned in section 4.1.1. Thus, particle turbulent diffusivity is proposed to be modeled as follows:

$$D_{tpdx1} = b_8 \times Re^{b_9} \times \mathrm{IE} \times D_{damp} \tag{4.14a}$$

$$D_{tpdx2} = b_8 \times Re^{b_9} \times \mathrm{CTE} \times \mathrm{IE} \times D_{damp} \tag{4.14b}$$

where b_8 and b_9 are parameters fitted using experimental data.

Particle-particle interaction flux in turbulent flows depends on collisions experienced by a particle due to turbulent fluctuations. This kind of flux also involves modeling of turbulence, hence turbulence has been incorporated in macroscopic way similar to particle turbulent diffusivity. The effect of particle shape and size is included using IE and CTE similar to turbulent dispersion flux. The effect of particle concentration has been modeled in the same way as shear viscosity is dependent on high concentration and maximum packing fraction (Schaan et al., 2000). Diffusivity due to particle-particle interaction is as follows:

$$D_{tppx1} = b_8 \times Re^{b_9} \times \mathrm{IE} \times \frac{b_7}{((\Phi_m/\Phi)^{1/3} - 1)^2} \tag{4.15a}$$

$$D_{tppx2} = b_8 \times Re^{b_9} \times \mathrm{CTE} \times \mathrm{IE} \times \frac{b_7}{((\Phi_m/\Phi)^{1/3} - 1)^2} \tag{4.15b}$$

Thus, complete particle diffusivity is as follows:

$$D_{tpx1} = b_8 \times Re^{b_9} \times \mathrm{IE} \times (D_{damp} + \frac{b_7}{((\Phi_m/\Phi)^{1/3} - 1)^2}) \tag{4.16a}$$

$$D_{tpx2} = b_8 \times Re^{b_9} \times \mathrm{CTE} \times \mathrm{IE} \times (D_{damp} + \frac{b_7}{((\Phi_m/\Phi)^{1/3} - 1)^2}) \tag{4.16b}$$

where b_7 is a parameter to be fitted using experimental data. Re is the flow Reynolds number.

Turbulence effects on scalar transport have been included in a macroscopic way, i.e particle dispersion depends on the mean flow and not in-situ velocity. It is expected that this assumption will work well as shear rates are negligible in turbulent flow except in the vicinity of the pipe wall. Shear rates near wall can lift the particle away from the wall as observed by Shook and Daniel (1965), but again this phenomenon is experienced only by large particles ($\geq 200\mu m$) (Wilson and Sellgren, 2003). Since the model assumptions are valid only for small particles, lift forces can

Reproduced with permission of the copyright owner. Further reproduction prohibited without permission.

also be safely neglected. Shear induced migration is negligible in turbulent flows as shear rates are negligible, while may become effective at high concentrations when turbulence is dampened; this condition is beyond those considered in this study and thus it can also be safely neglected.

4.2 Slurry Flow Modeling : Tuning

All the transport equations have been developed for the pipeline cross-section as shown in Figure 4.1. The cross-section is symmetric about x_2-direction, hence equations were solved only in one half of the circle. Symmetric boundary conditions were imposed on x_2-direction, with the remaining boundaries unchanged as they represent pipeline wall. These equations were solved using Finite Element Method Software COMSOL Multiphysics. The unknown parameters were fitted using MATLAB and trial and error. Scalar transport equation uses averaged turbulence effects, and hence is independent of in-situ velocity. Thus, parameters of scalar transport equation were solved independent of those in turbulent viscosity model.

4.2.1 Scale-up Effects

After curve fitting the parameters of viscosity and scalar transport models an under prediction of pressure drop was observed. Hence, a factor was included in turbulent viscosity to incorporate for scale-up. The empirical dependence of slurry turbulent viscosity on Re was derived using single phase equations and friction factor from Colebrook relation as described in Section 4.1.1. This procedure incorporates only for interaction between fluid and wall. Interactions between wall and particles were included by the scale-up factor, which is an empirical addition. This effect is proposed to be modeled using Froude Number as follows:

$$Fr_s^{b_5} = (\frac{gD_t}{U_{avg}^2})^{b_5} \tag{4.17}$$

Reproduced with permission of the copyright owner. Further reproduction prohibited without permission.

The final expression for turbulent viscosity is as follows:

$$\begin{aligned} \text{Slurry Turbulent Viscosity} &= \text{Turbulent Viscosity Of Fluid} \\ &\times \text{Turbulence Modulation} \\ &\times \text{Particle Characteristics} \\ &\times \text{Scale-up Effects} \end{aligned} \tag{4.18}$$

While fitting the concentration distribution, the parameters were fitted to incorporate the effects of particle size, concentration and scale-up in the model. Similarly, turbulent viscosity parameters were fitted using experimental data on pressure drop to incorporate the effects of particle size, concentration and scale-up. Figure 4.4 and Figure 4.5 compares the model predictions with experimental data used in parameter fitting. In the current study while comparing the model predictions with experimental data the graphs have been plotted in the following way:

Pressure drop comparison graphs In a graph comparing pressure drop predictions of the model with experimental data, abscissa shows varying mean flow rate (U_{avg}) in m/s and ordinate shows pressure drop in kPa/m. Different pressure drop profiles have been plotted against mean flow rate with varying average concentration of particles (Φ_p).

Concentration profile comparison graphs In a graph comparing concentration profile predictions from a model with experimental data, abscissa denotes the volume fraction of particles and ordinate denotes dimensionless elevation in a pipeline (y/D), hence it varies from 0 to 1 only. Different concentration profiles have been plotted against dimensionless elevation in pipeline either with varying average concentration of particles (Φ_p) or mean flow rate (U_{avg}).

Table 4.1 summarises the experimental data set used for tuning and validation of model. The comments provide information about the type of experimental data available in those conditions or the type of particles constituting the slurry. The number of parameters fitted were ten and six kinds of data sets were used with varying U_{avg} and Φ_p. The values of all the parameters are given in Appendix B along with the detailed model equations.

Reproduced with permission of the copyright owner. Further reproduction prohibited without permission.

Data Set	Tuning or Validation	Study	D_t (mm)	d_p μm	Notes
1	T	Other [1]	100	190	Concentration
2	TV	Other [1]	100	90	Concentration
3	TV	Gillies (1993)	159	190	Concentration
4	T	Schaan et al. (2000)	50	85	Pressure drop
5	T	Roco and Shook (1984)	50	165	Pressure drop
6	T	Roco and Shook (1984)	250	165	Pressure drop
7	V	Gillies et al. (2004)	100	90	LM125 particles
8	V	Schaan et al. (2000)	50	90	Broad particle distribution
9	V	Schaan et al. (2000)	150	90	Broad particle distribution
10	V	Schaan et al. (2000)	50	100	Pressure drop
11	V	Gillies (1993)	500	180	Concentration
12	V	Gillies (1993)	53	180	Pressure drop and concentration
13	V	Roco and Shook (1984)	500	165	Pressure drop
14	V	Gillies et al. (2004)	103	270	Pressure drop and concentration

Table 4.1: Experimental data used for tuning and validation of model

4.3 Slurry Flow Modeling : Validation

The mixture model developed using the pseudo-homogenous mixture assumption was tested with the experimental data that have been published by SRC over the years. The experimental data set is constrained in the range of particle size by two assumptions made in the model, i.e turbulence dampening on addition of particles to the carrier fluid and insignificant lift force experienced by particles. The particle size chosen ranges from $90\mu m$ to $270\mu m$. This range of particle diameter also illustrates the limitations of the model. The chosen experimental data set has a narrow particle size distribution, thus d_{50} is taken as the particle size of the sample. However most of the data sets with narrow particle size distribution, have a similar maximum packing fraction, thus it became difficult to study the effect of particle shape. Nonetheless a data set on broad particle distribution has been included which has a significantly different Φ_m from the remaining data set, which helps to study

Reproduced with permission of the copyright owner. Further reproduction prohibited without permission.

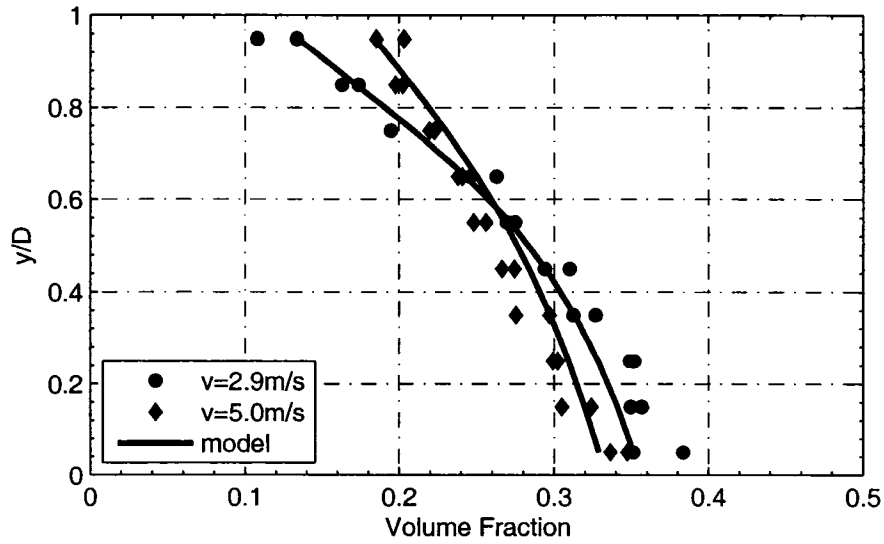

(a) Concentration profile with elevation D_t=100mm, d_p=190μm,Φ_p=0.27

Figure 4.4: Model predictions as compared to experimental results for data used in fitting parameters for particle transport, data set 1

the effect of particle shape (data set 8 and 9). The model has been compared with the experimental measurements of following:

1. Variation of chord averaged particle concentration in the vertical direction. The experimental data available in the literature on concentration profile are measured along 10 horizontal chords in vertical direction.

2. Velocity profile along central vertical plane, i.e. along the direction of gravity. The velocity profile has been measured at the central vertical plane for the slurry.

3. Pressure drop in the slurry pipeline. Pressure drop measurements are made along a known pipeline length in the fully developed region.

Figure 4.6a compares pressure drop predictions for data set 7. Φ_p varies from 0.19 to 0.33. The model predictions show a good agreement with the experimental measurements. An increasing difference between the predictions and experimental results has been observed with increasing flow rate. This is because as the flow

[1]Courtesy Dr. S. Sanders at University of Alberta and Dr. J. Schaan at Syncrude Canada Ltd.

Reproduced with permission of the copyright owner. Further reproduction prohibited without permission.

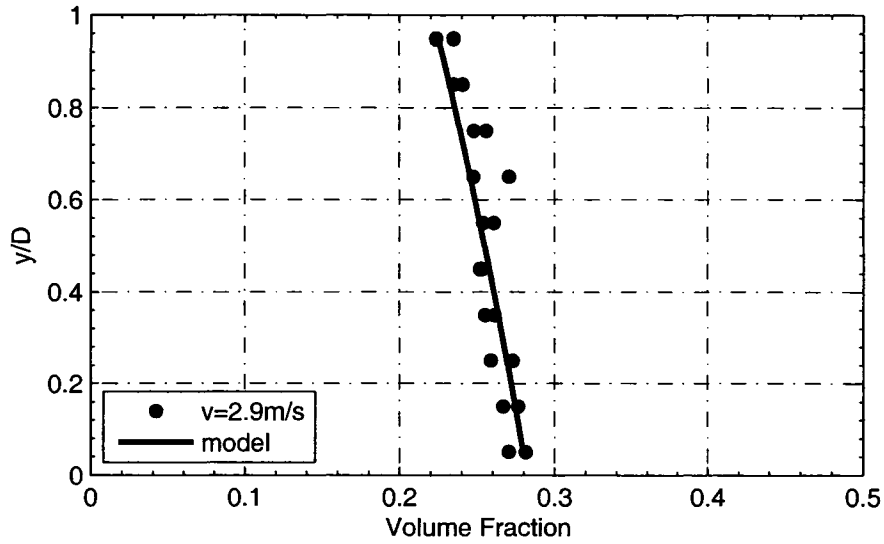

(b) Concentration profile with elevation D_t=100mm, d_p=90μm,Φ_p=0.254, data set 2

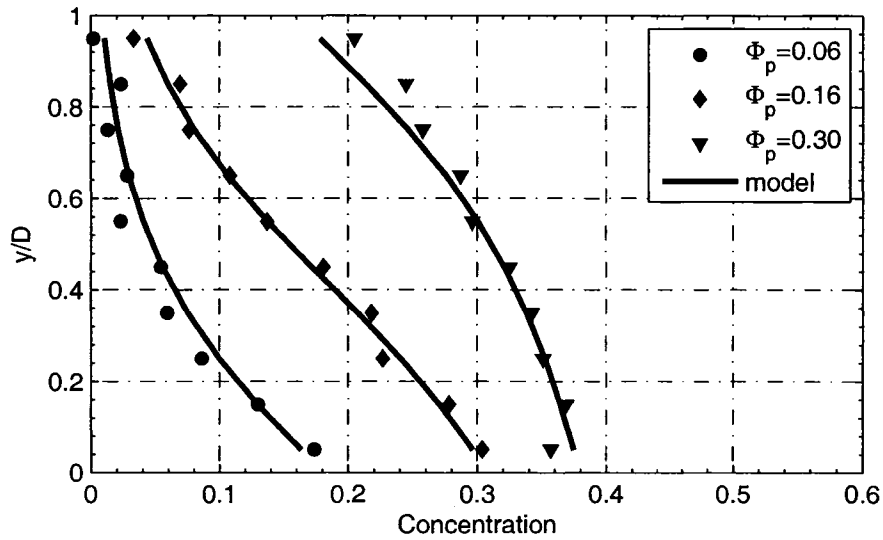

(c) Concentration profile with elevation D_t=159mm, d_p=190μm,U_{avg}=2.75m/s, data set 3

Figure 4.4: Model predictions as compared to experimental results for data used in fitting parameters for particle transport (cont'd)

rate increases the particle experiences lift off from the wall, as observed by Wilson and Sellgren (2003) and Gillies et al. (2004). Thus lift forces also play role in suspending the particles. Hence, pressure drop reduces and over prediction by the model is observed.

Reproduced with permission of the copyright owner. Further reproduction prohibited without permission.

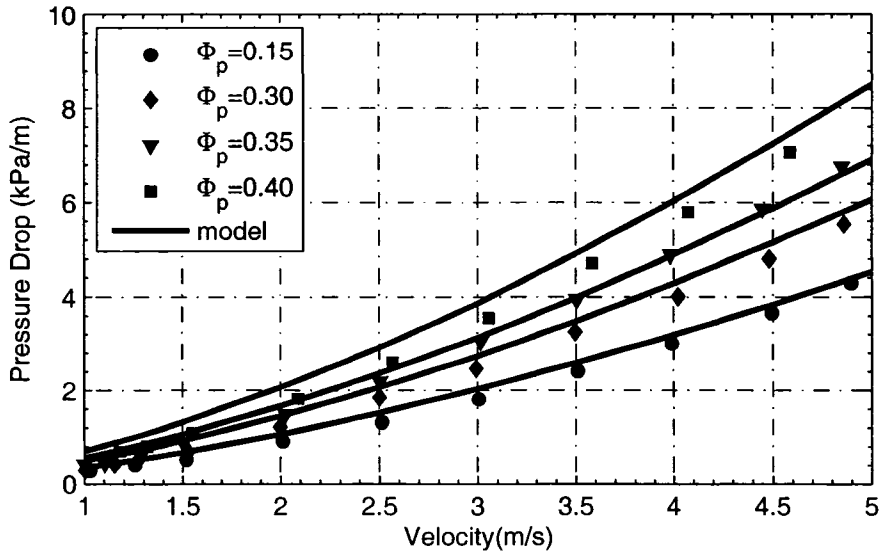

(a) Pressure drop vs velocity, D_t=50mm,d_p=85μm, data set 4

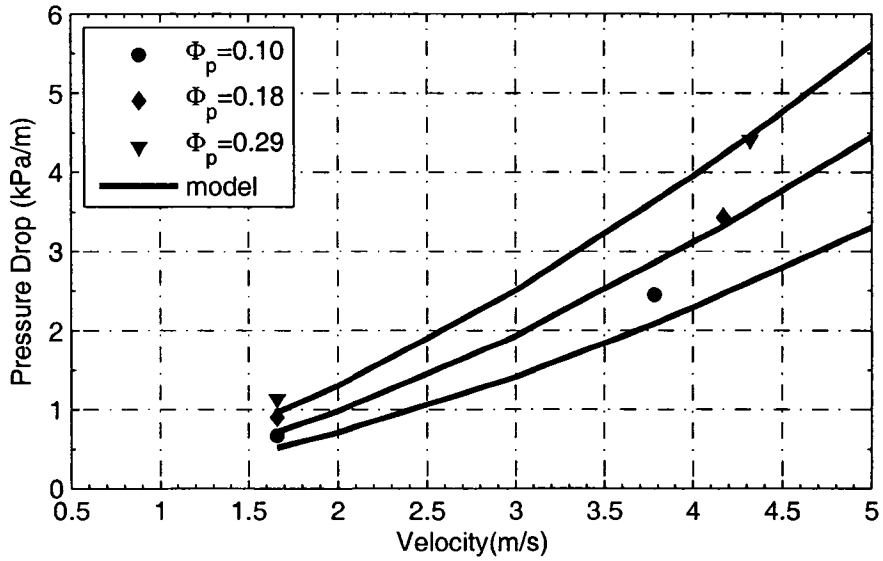

(b) Pressure drop vs velocity, D_t=50mm,d_p=165μm, data set 5

Figure 4.5: Model predictions as compared to experimental results for data used in fitting parameters for mixture turbulent viscosity

Figure 4.6b compares concentration predictions with varying Φ_p at U_{avg} =3m/s for data set 7. Since flow rate is above the deposition velocity ($U_{avg}/U_c \geq 2$), model predictions agree well with the experimental measurements. A small increase in

Reproduced with permission of the copyright owner. Further reproduction prohibited without permission.

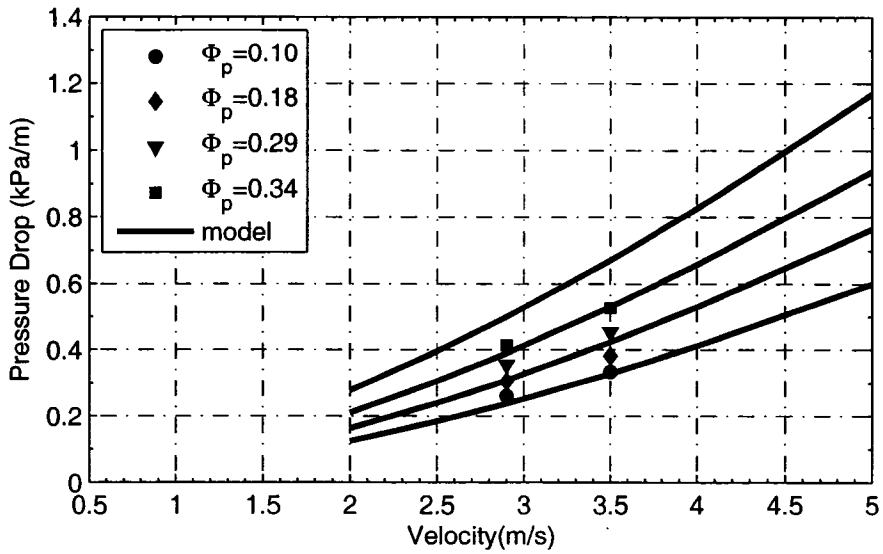

(c) Pressure Drop vs Velocity, D_t=250mm,d_p=165μm, Data Set 6

Figure 4.5: Model predictions as compared to experimental results for data used in fitting parameters for mixture turbulent viscosity (cont'd)

suspension uniformity has been observed with increasing Φ_p. This occurs due to the increase in particle-particle interaction with Φ_p. Figure 4.7 compares pressure gradient predictions for data sets 8 and 9. It shows that model predictions agree well with the experimental observations on increasing the pipeline diameter for small sized particles.

Figures 4.7a and 4.7c show pressure drop predictions for data sets 8 and 10. Φ_m for data set 10 is 0.622 and for data set 8 is 0.505. For Φ_p =0.15 pressure gradients in the two slurries are almost identical. But as Φ_p increases pressure gradients in data set 8 increase. For Φ_p =0.35 and U_{avg} >1.5m/s, pressure drop predictions for data set 10 are consistently less than that of data set 8. This difference in the pressure gradients arises due to two factors i.e. particle size and shape. As particle size increases, settling tendency of particles increases and hence pressure drop increases. But a reverse trend has been observed in this comparison which shows that particle shape is significantly affecting pressure drop. Particle shape changes Φ_m; as Φ_m increases, for similar flow conditions, slurry turbulent viscosity decreases and so does pressure drop. The model predictions closely agree with the experimental

Reproduced with permission of the copyright owner. Further reproduction prohibited without permission.

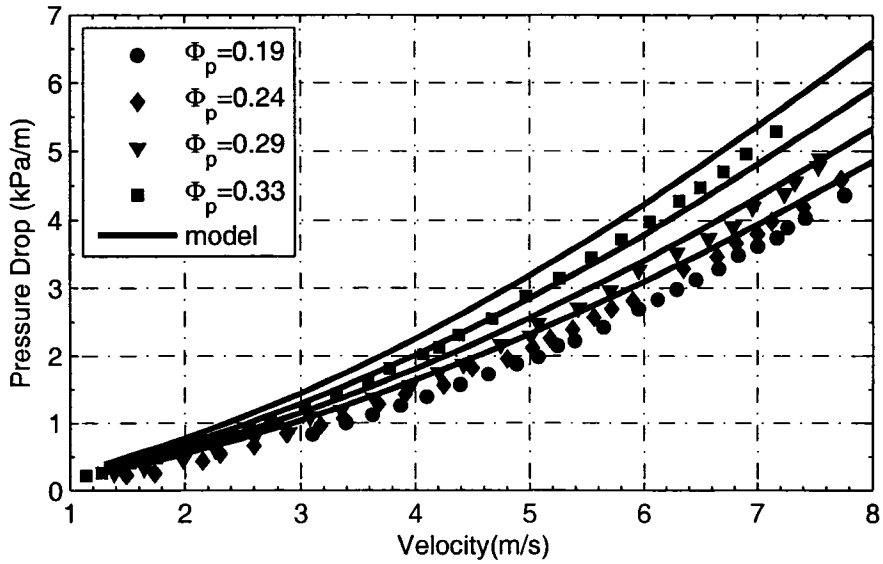

(a) Pressure drop vs velocity for D_t = 100mm, d_p = 90μm

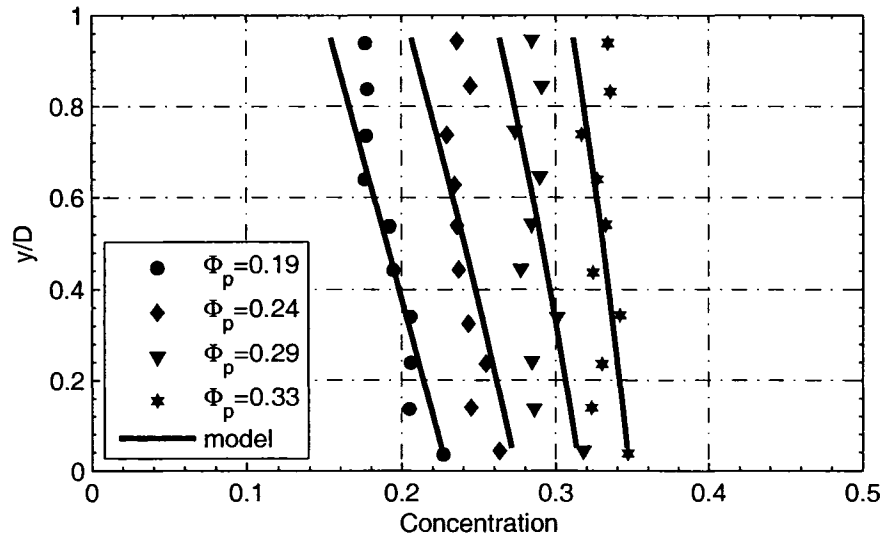

(b) Concentration profile with elevation for D_t = 100mm, d_p = 90μm,U_{avg} = 3m/s

Figure 4.6: Pressure drop and concentration predictions for d_p = 90μm and D_t = 100mm, data set 7

Reproduced with permission of the copyright owner. Further reproduction prohibited without permission.

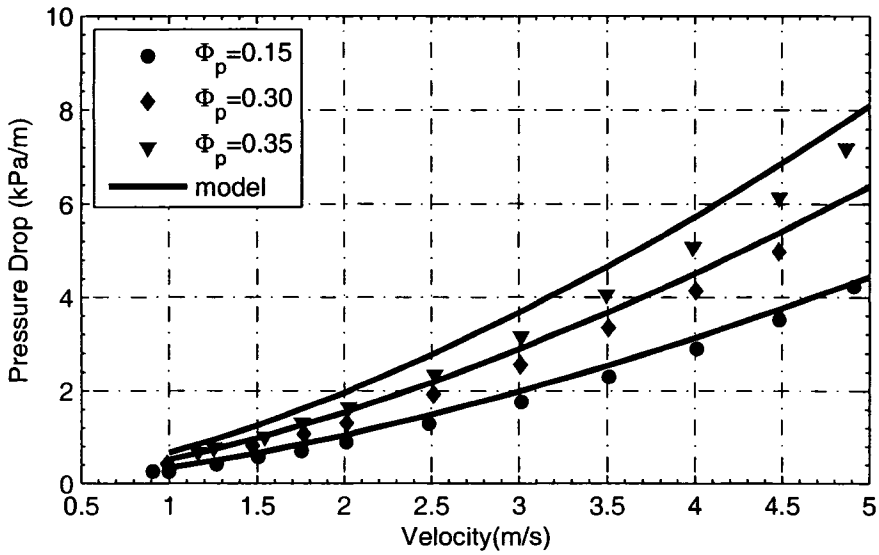

(a) Pressure drop vs velocity for D_t = 50mm, d_p = 90μm, Φ_m = 0.505, data set 8

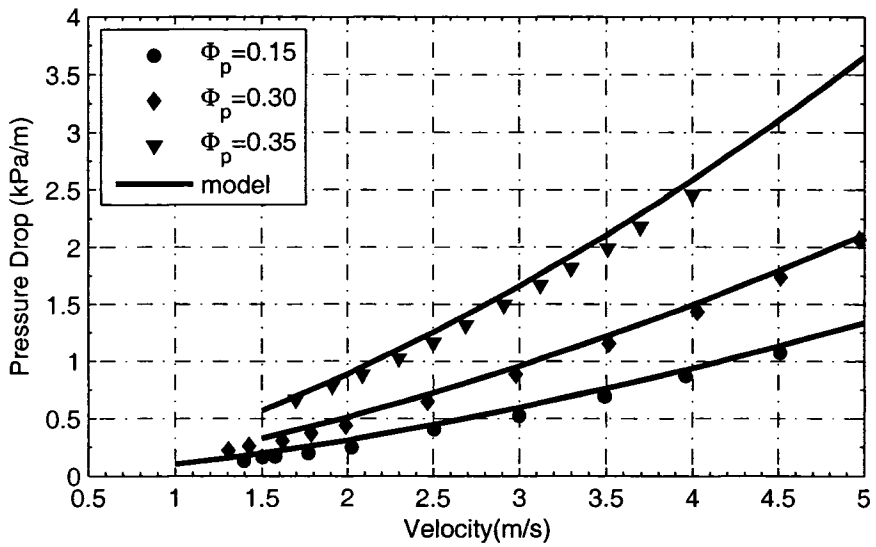

(b) Pressure Drop vs Velocity for D_t = 150mm, d_p = 90μm, Data Set 9

Figure 4.7: Effect of scale-up on broad particle size distribution

Reproduced with permission of the copyright owner. Further reproduction prohibited without permission.

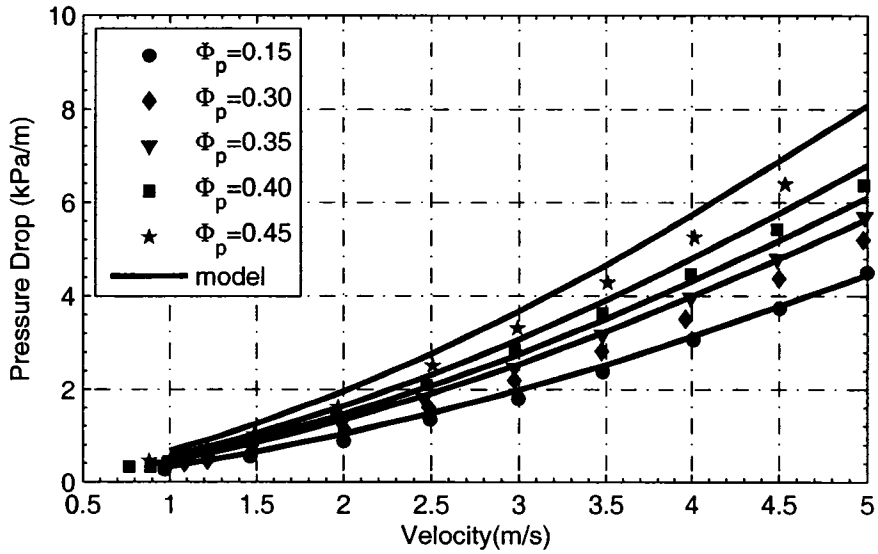

(c) Pressure Drop vs Velocity for D_t = 50mm, d_p = 100μm, Φ_m = 0.622, data set 10

Figure 4.7: Effect of particle shape

results.

Figures 4.8-4.10 compare model predictions for concentration and pressure gradients for larger particles, i.e. 180μm and 190μm with a narrow size distribution in pipelines varying from 50mm to 500mm. Figure 4.8 shows concentration profiles for data sets 3 and 11 near deposition velocity for 190μm and 180μm respectively. At low $\Phi_p \leq 0.15$, model predictions do not conform with the experimental measurements at the bottom of the pipeline and suggests a relatively more dispersed system than observed. However, as Φ_p increases model predictions agrees well with the experimental observations. At low Φ_p, lift forces are also significant compared to the particle-particle interaction, but as Φ_p increases particle-particle interaction increases rapidly and leads to a more uniformly dispersed slurry. Figure 4.9 shows concentration distributions for data set 12, with flow rate well above the deposition velocity. As U_{avg} and Φ_p increases, turbulent dispersion and particle-particle interaction flux increases respectively and leads to more uniform distribution of particles.

Figures 4.10a and 4.10b shows pressure drop predictions for data sets 13 and 12 respectively. Model predictions show a reasonable match with the experimental

Reproduced with permission of the copyright owner. Further reproduction prohibited without permission.

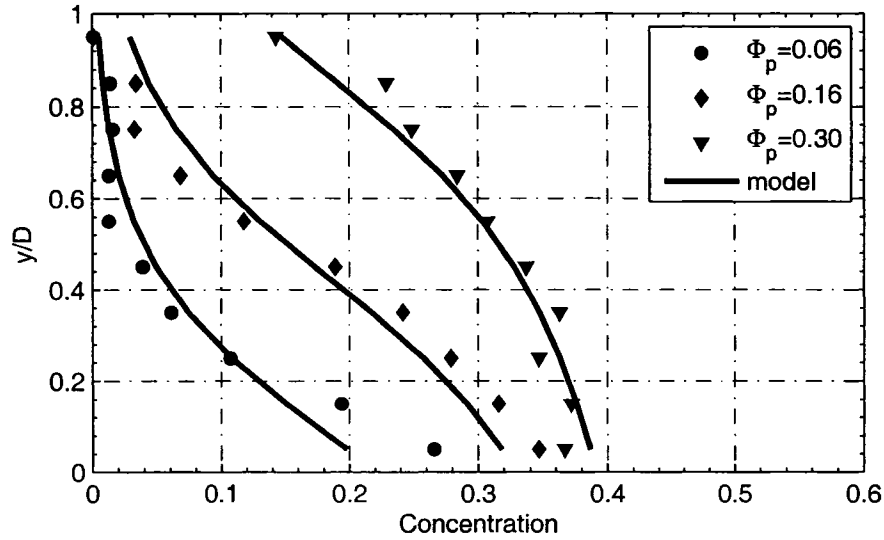

(a) Concentration profile with elevation for D_t = 159mm, d_p = 190μm,U_{avg} = 2.74m/s, data set 3

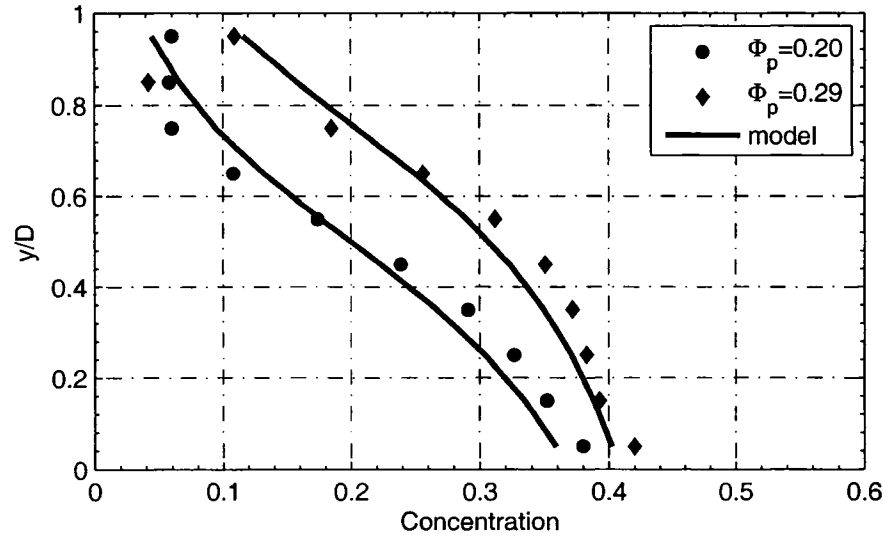

(b) Concentration profile with elevation for D_t = 500mm, d_p = 180μm,U_{avg} = 3.1m/s, data set 11

Figure 4.8: Concentration profiles in the vicinity of deposition velocity

Reproduced with permission of the copyright owner. Further reproduction prohibited without permission.

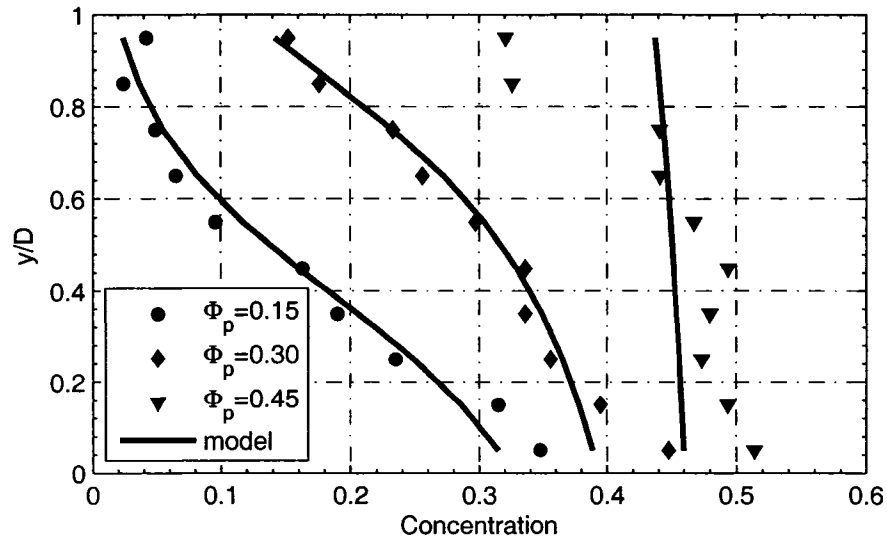

(a) Concentration profile with elevation for D_t = 53mm, d_p = 180μm,U_{avg} = 1.8m/s, data set 12

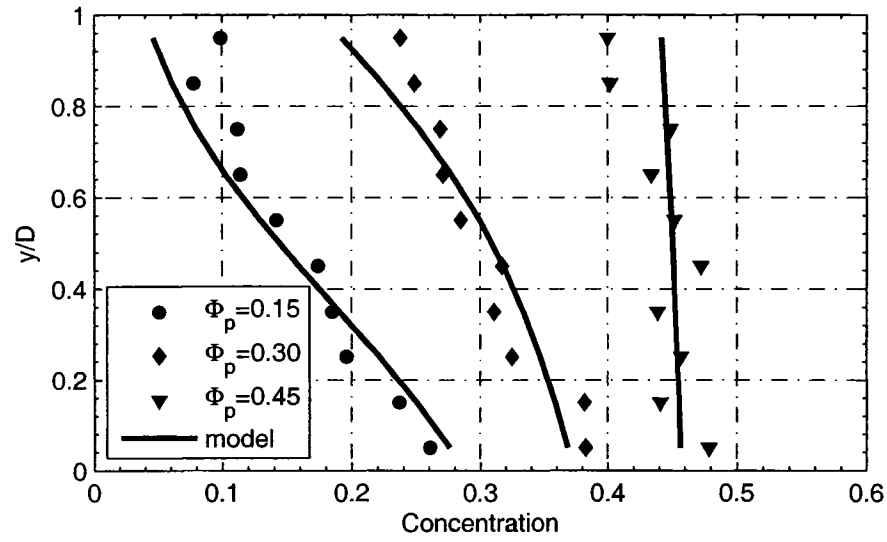

(b) Concentration profile with elevation for D_t = 53mm, d_p = 180μm,U_{avg} = 3.1m/s, data set 12

Figure 4.9: Concentration profiles above deposition velocity

Reproduced with permission of the copyright owner. Further reproduction prohibited without permission.

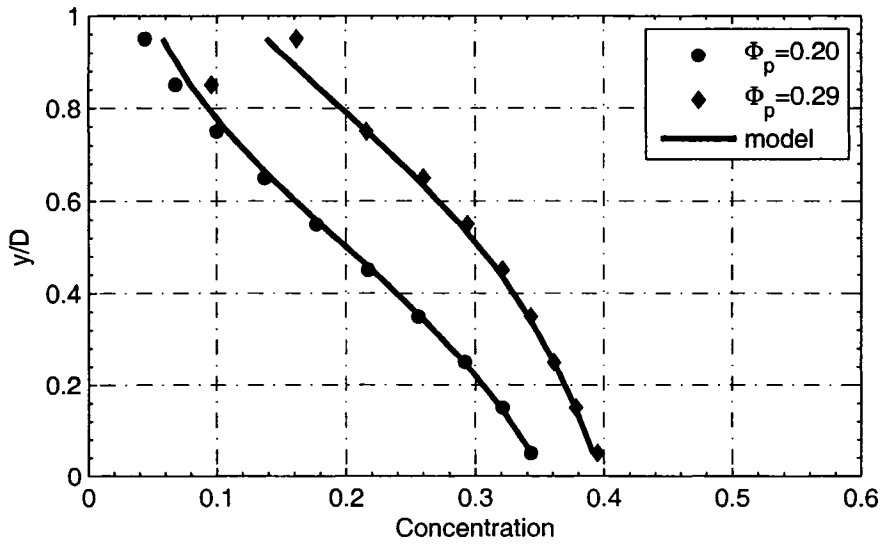

(c) Concentration profile with elevation for D_t = 500mm, d_p = 180μm,U_{avg} = 3.8m/s, data set 11

Figure 4.9: Concentration profiles above deposition velocity (cont'd)

results on scale-up for larger particles. However, for 180μm particles the deviations in pressure drop predictions from experimental observations increases considerably at Φ_p =0.45. This has been observed due to inappropriate modeling of turbulent viscosity dependence on particle concentration and shape and also due to inappropriate modeling of turbulence dampening. At this high concentration, significant turbulence damping occurs resulting in reduced pressure gradients (Schaan et al., 2000). The exponential function of turbulence dampening is insufficient at high concentrations (Roco and Shook, 1984).

The model is also checked with $d_p = 270\mu m$ in a 103mm pipeline. The model over predicts pressure drop as shown in Figure 4.11a. This is because of following reasons.

1. Due to the increase in particle size, the settling velocity of particles is quite high, hence the assumption of no-slip between solid and liquid might fail. Moreover, a particle size between 200μm-500μm experiences lift from the wall which reduces pressure drop (Wilson and Sellgren, 2003).

2. The assumption of turbulence attenuation is limited only for particle size $d_p <$

Reproduced with permission of the copyright owner. Further reproduction prohibited without permission.

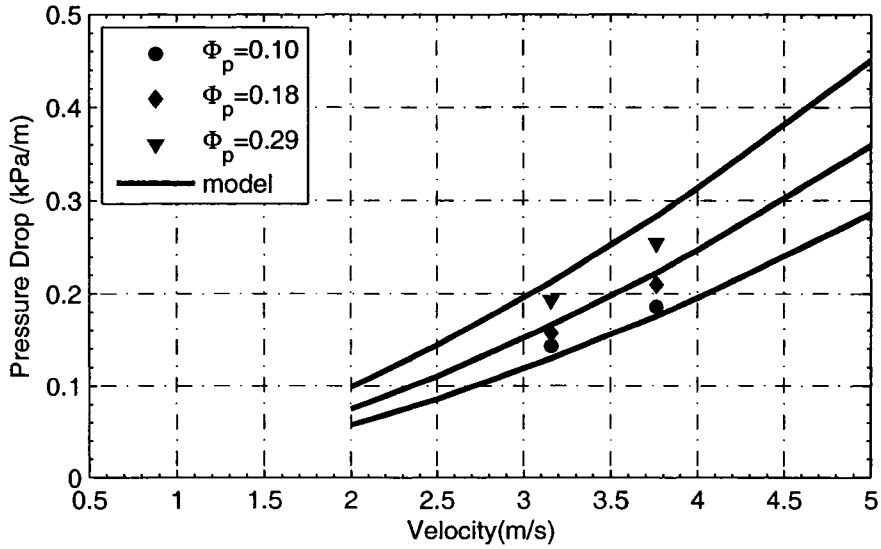

(a) Pressure drop vs velocity for D_t = 500mm, d_p = 165μm, data set 13

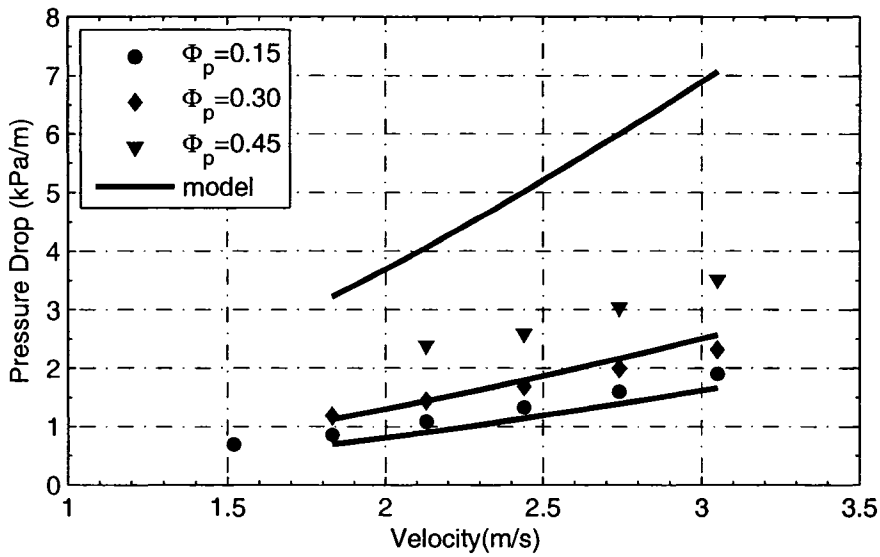

(b) Pressure drop vs velocity for D_t = 50mm, d_p = 180μm, data set 12

Figure 4.10: Effect of scale-up II

Reproduced with permission of the copyright owner. Further reproduction prohibited without permission.

$250\mu m$, hence dependence on particle size is not appropriately modeled.

3. The model highly over predicts pressure gradient at high concentration because of the sudden increase in turbulence dampening as mentioned earlier.

All the above factors lead to over prediction of pressure drop and show that the poor model predictions are to be expected.

Figure 4.11b compares concentration predictions for data set 14. The model qualitatively follows the behaviour and shows an increase in suspension uniformity with Φ_p. Model predictions for the concentration at the pipe bottom agrees well with experimental results. But on moving upwards in the pipeline, a sudden fall in the concentration has been observed, contrary to the experimental observations. This can be explained as follows: as particle size increases settling velocity increases. At the bottom of the pipeline, the model balances gravitational force by particle-particle interaction force due to high in-situ Φ. Until y/D ≤ 0.3 this phenomenon has been observed; above that turbulent dispersion force balances the gravitational force. This shows that turbulent dispersion and particle-particle interaction flux are not the only phenomena leading to particle dispersion in the pipeline. Thus, an appropriate lift model has to be incorporated. Turbulence has been incorporated in a macroscopic way in the momentum equation, i.e. it is dependent on the mean flow rate and not on in-situ velocity. Hence, momentum equation in axial direction is mathematically equivalent to laminar flow of a highly viscous fluid.

Figure 4.12 represents velocity profile along the central vertical plane with varying U_{avg} for data set 7. As mean flow rate is increased, slurry becomes more uniformly suspended and makes the flow more symmetric, which has been observed in Figure 4.12. The velocity profiles in Figure 4.12, both experimental measurements and model predictions, when integrated upon the pipeline cross-section (Figure 4.1), gives equal flow rate. As mentioned earlier, the velocity profiles are parabolic similar to highly viscous laminar flows. Thus, better turbulence model for momentum balance has to be incorporated.

Reproduced with permission of the copyright owner. Further reproduction prohibited without permission.

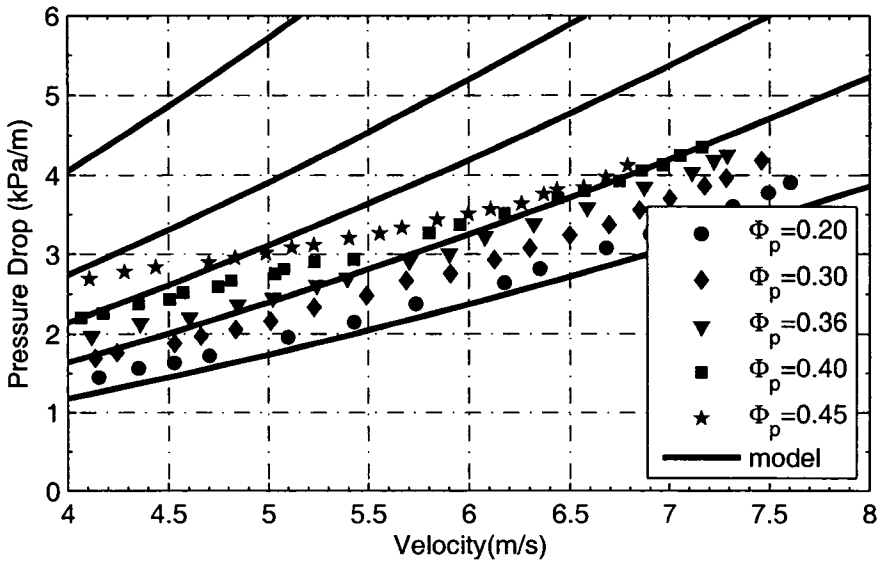

(a) Pressure drop vs velocity for D_t = 103mm, d_p = 270μm

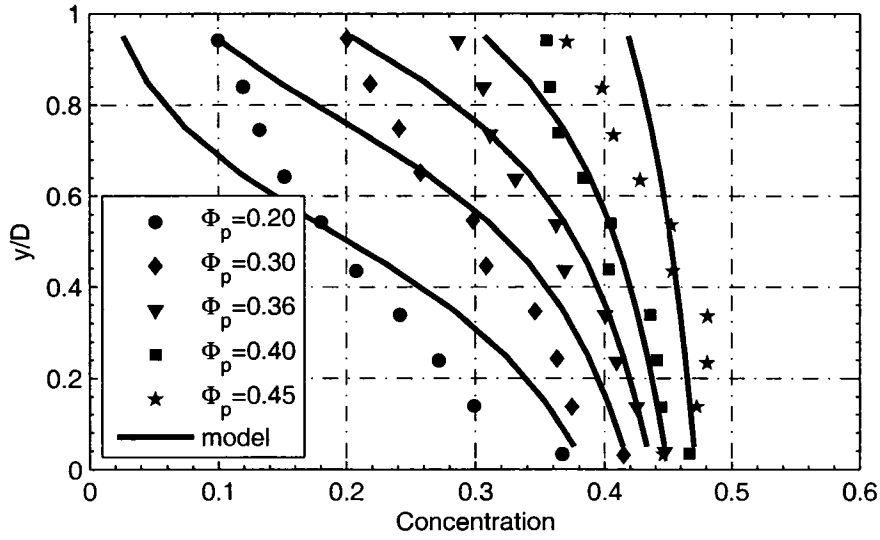

(b) Concentration profile with elevation for D_t = 100mm, d_p = 270μm,U_{avg} = 5.4m/s

Figure 4.11: Pressure drop and concentration profile for d_p = 270μm and D_t = 100mm, data set 14

Reproduced with permission of the copyright owner. Further reproduction prohibited without permission.

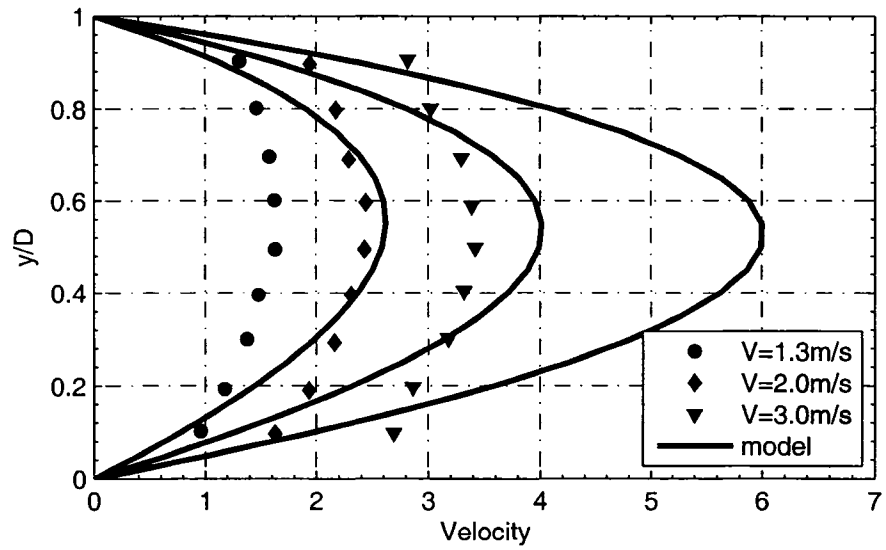

Figure 4.12: Velocity profile with vertical position for D_t = 103mm, d_p = 90μm and Φ_p = 0.19 data set 7

Reproduced with permission of the copyright owner. Further reproduction prohibited without permission.

Chapter 5

Conclusions and Recommendations

The performance of the piston sampler as technique to measure BSD can be summarised as follows:

1. BSD's from piston sampler are invariant with different air−water flow rates, and do not agree with BSD's measured from photographic technique. This shows that piston sampling does fail at low air−water flow rates either because piston is breaking the bubbles or the piston centering is capturing bubbles from a position where bubble size does not change significantly with small changes in air−water flow rates.

2. Due to the physical constraints of the existing set-up and BSD measurement techniques, there is a small regime of air−water flow rates where piston sampling can be checked with photographic technique. The physical constraints should be removed in the future by redesigning the pump and stand tank to handle higher air and water flow rates.

3. Future experiments should be conducted at higher water flow rates to operate in the break-up dominant regime where equilibrium consists of monodispersed bubble sizes. This will help in removing the effect of centering of the sampler and also the bubbles will be smaller and spherical, hence the photographic technique is more likely to provide a good basis for comparison.

The performance of the pseudo-homogeneous mixture model developed here and tested against pre-existing experimental data can be summarised as follows:

Reproduced with permission of the copyright owner. Further reproduction prohibited without permission.

1. The concept of turbulent viscosity of slurry has been introduced and has been modeled as a product of turbulent viscosity of carrier fluid, turbulence modulation and effect of particle shape and concentration.

2. A new model for flux due to particle fluctuations in turbulent flows has been proposed by considering turbulence in a macroscopic sense and using the concept of minimum distance between particles at maximum packing fraction (Schaan et al., 2000).

3. Concentration predictions agree well with the experimental data for U_{avg}/U_c >1.2. Model over predicts the suspension uniformity for U_{avg}/U_c <1.2. The model agrees well with the experimental data available for $d_p \leq 250\mu m$ in all the pipe sizes, i.e 50-500mm. Model predictions of concentration distribution for $d_p > 250\mu m$ do not agree with experimental results as turbulent dispersion and particle-particle interactions are insufficient to disperse the particles.

4. Pressure drops have been predicted successfully using slurry turbulent viscosity within the range of its validity. The model predictions agrees well in pipe size of 50 mm for varying particle sizes i.e $85\mu m - 180\mu m$ and also helps in studying the effects of particle shape through maximum packing fraction. The model shows an inconsistent behaviour around deposition velocity. The scale-up effects included in the model is entirely empirical and model shows over prediction for pipe sizes above 150mm. Pressure drop predictions fail at high concentration when particles considerably dampen turbulence, as seen in data set 12 at $\Phi_p = 0.45$.

5. The turbulence modulation model proposed here is inappropriate for high concentration and larger particles. At present it is difficult to model the criterion for significant turbulence dampening. More experimental measurements of pressure drops are needed to understand dampening with respect to concentration of particles.

6. The model is limited because it does not consider lift force and a universal model for turbulence modulation. However, this model provides a basis for

Reproduced with permission of the copyright owner. Further reproduction prohibited without permission.

a particle-particle interaction model which can be incorporated in CFD software by modifying turbulent dispersion coefficient through user subroutines to formulate a complete 3-D model.

Reproduced with permission of the copyright owner. Further reproduction prohibited without permission.

Bibliography

A. Acrivos, R. Mauri, and X. Fan. Viscous resuspension of a sediment within a laminar and stratified flow. *International Journal of Multiphase Flow*, 19(5): 797–802, 1993.

R. A. Bagnold. Experiments on a gravity-free dispersion of large solid spheres ina newtonian fluid under shear. *Proc. Roy. Soc., Ser. A.*, 225:4–=63, 1954.

R. A. Bagnold. Flow of cohesionless grains in fluids. *Philosophical Transactions, Royal Society, London*, 249, 1956.

M. Barigou and M. Greaves. A capillary suction probe for bubble size measurement. *Measurement Science and Technology*, 2:318–326, 1991.

C. Boyer, A.-M. Duquenne, and G. Wild. Measuring techniques in gas-liquid and gas-liquid-solid reactors. *Chemical Engineering Science*, 57:3185–3215, 2002.

A. Cartelier and J. L. Achard. Local phase detection probes in fluid-fluid two-phase flows. *Review of Scientific Instruments*, 62(2):279–303, 1991.

C. O. Chen and P. E. Wood. Turbulence closure models for dilute gas-particle flows. *Canadian Journal of Chemical Engineering*, 63:349–360, 1985.

F. Chen, C. O. Gomez, and J. A. Finch. Technical note bubble size measurement in flotation machines. *Minerals Engineering*, 14(4):427–432, 2001.

C. T. Crowe. On models for turbulence modulation in fluid-particle flows. *International Journal of Multiphase Flow*, 26:719–727, 1999.

C. T. Crowe, T. R. Troutt, and J. N. Chung. Numerical models for two-phase flows. *Annual Review of Fluid Mechanics*, 28:11–43, 1996.

Reproduced with permission of the copyright owner. Further reproduction prohibited without permission.

H. DeLasa, S. L. P. Lee, and M. A. Bergougnou. Bubble measurement in 3-phase fluidized-beds using a u-shaped optical fiber. *Canadian Journal of Chemical Engineering*, 62(2):165–169, 1984.

S. Elghobhashi. On predicting particle-laden turbulent flows. *Appl. Sci. Res*, 52: 309–329, 1994.

D. Eskin, Y. Leonenko, and O. Vinogradov. Theoretical estimates of air bubble behavior in dense pipeline slurry flows. *Chemical Engineering and Processing*, 43:727–737, 2004.

R. G. Gillies. *Pipeline Flow of Coarse Particle Slurries*. PhD thesis, University of Saskatchewan, Saskatoon, SK, 1993.

R. G. Gillies, C. A. Shook, and J. Xu. Modelling heterogeneous slurry flows at high velocities. *Canadian Journal of Chemical Engineering*, 82:1060–1065, October 2004.

R. A. Gore and C. T. Crowe. Effect of particle size on modulation turbulence intensity. *International Journal of Multiphase Flow*, 15:279–285, 1989.

G.W. Govier and K. Aziz. *The Flow of Complex Mixtures in Pipes*. Van Nostrand Reinhold Co., New York, NY, 1972.

R. P. Hesketh, A. W. Etchells, and T. W. F. Russell. Bubble size in horizontal pipelines. *AIChE Journal*, 33:663, 1987.

R. P. Hesketh, A. W. Etchells, and T. W. F. Russell. Experimental observations of bubble breakage in turbulent flow. *Ind. Eng. Chem. Res.*, 30:835–841, 1991a.

R. P. Hesketh, A. W. Etchells, and T. W. F. Russell. Bubble breakage in pipeline flow. *Chemical Engineering Science*, 46(1):1–9, 1991b.

P.N. Holtham. Particle transport in gravity concentrators and the bagnold effect. *Minerals Engineering*, 5(2):205–221, 1992.

Reproduced with permission of the copyright owner. Further reproduction prohibited without permission.

F. L. Hsu, R. M. Turian, and T. W. Ma. Flow of noncolloidal slurries in pipelines. *AICHE Journal*, 35(3):429–442, 1989.

M. Ishida and H. Tanaka. An optical probe to detect both bubbles and suspended particles in a 3-phase fluidized-bed. *Journal Of Chemical Engineering Of Japan*, 15(5):389–391, 1982.

V. M. Kenning and C. T. Crowe. On the effect of particles on carrier phase turbulence in gas-particle flow. *International Journal of Multiphase Flow*, 23:403–408, 1997.

J. C. Lasheras, C. Eastwood, C. Martínez-Bazán, and J. L. Montañés. A review of statistical models for the break-up of an immiscible fluid immersed into fully developed trubulent flow. *International Journal of Multiphase Flow*, 28:247–278, 2001.

D. Leighton and A. Acrivos. Viscous resuspension. *Chemical Engineering Science*, 41(6):1377–1384, 1985.

D. Leighton and A. Acrivos. The shear-induced migration of particles in concentrated suspensions. *Journal of Fluid Mech.*, 181:415–430, 1987a.

D. Leighton and A. Acrivos. Measurement of shear-induced self-diffusion in concentrated suspensions of spheres. *Journal of Fluid Mech*, 177:109–131, 1987b.

M. F. Lightstone and S. M. Hodgson. Turbulence modulation in gas-particle flows: A comparison of selected models. *Canadian Journal of Chemical Engineering*, 82:209–219, April 2004.

J. Ling, P. V. Skudarnov, C. X. Lin, and M. A. Ebadin. Numerical invetsigations of liquid-solid slurry flows in a fully developed turbulent flow region. *International Journal of Heat and Fluid Flow*, 24:389–398, 2003.

M. Luthra, R. J. G. Lopetinsky, R. S. Sanders, K. Nandakumar, and J. H. Masliyah. A new device to determine bitumen extraction from oil sands. *Canadian Journal of Chemical Engineering*, 82:752–762, August 2004.

Reproduced with permission of the copyright owner. Further reproduction prohibited without permission.

K. Malysa, S. Ng, L. Cymbalisty, J. Czarnecki, and J. Masliyah. A method of visualisation and characterisation of aggregates flow inside a separation vessel. i. size, shape and rise velocity of the aggregates. *International Journal of Mineral Processing*, 55:171–188, 1999.

C. Martinez-Bazan, J. L. Montañés, and J. C. Lasheras. On the breakup of an air bubble injected into a fully developed turbulent flow. part i. breakup frequency. *Journal of Fluid Mechanics*, 401:157–182, 1999a.

C. Martinez-Bazan, J. L. Montañés, and J. C. Lasheras. On the breakup of an air bubble injected into a fully developed turbulent flow. part ii. size pdf of the resulting daughter bubbles. *Journal of Fluid Mechanics*, 401:183–207, 1999b.

J. Masliyah, Z. Zhou, Z. Xu, J. Czarnecki, and H. Hamza. Understanding water-based bitumen extraction from athabasca oil sands. *Canadian Journal of Chemical Engineering*, 82:628–654, August 2004.

A. Matsuura and L. S. Fan. Distribution of bubble properties in a gas-liquid-solid fluidized-bed. *AIChE Journal*, 30(6):894–903, 1984.

B. Mols and R. V. A. Oliemans. A turbulent diffusion model for particle dispersion and deposition in horizontal tube flow. *International Journal of Multiphase Flow*, 24(1):55–75, 1998.

A. A. Mostafa and H. C. Mongia. On the intraction of particles and turbulent fluid flow. *International Journal of Heat and Mass Transfer*, 31(10):2063–2075, 1988.

R. J. Philips, R. C. Armstrong, R. A. Brown, A. L. Graham, and J. R. Abbott. A constitutive equation for concentrated suspensions that accounts for shear-induced particle migration. *Physics Fluids A*, 17(4):469–483, 1991.

F. Pourahmadi and J. A. C. Humphrey. Production and dissipation of energy in the turbulent flow of a particle-fluid mixture, with some results on drag reduction. *PCH Physicochemical Hydrodynamics*, 4(3):191, 1983.

Reproduced with permission of the copyright owner. Further reproduction prohibited without permission.

H. M. Prasser, A. Bottger, and J. Zschau. A new electrode-mesh tomograph for gas-liquid flows. *Flow Measurement and Instrumentation*, 9:111–119, 1998.

H. M. Prasser, D. Schollz, and C. Zippe. Bubble size measurement using wire-mesh sensors. *Flow Measurement and Instrumentation*, 12:299–312, 2001.

M. J. Prince and H. W. Blanch. Bubble coalescence and break-up in air-sparged bubble-columns. *AIChE Journal*, 36(10):1485–1499, 1990.

M. M. Razzaque, A. Afacan, S. Liu, K. Nandakumar, J. H. Masliyah, and R. S. Sanders. Bubble size in coalescence dominant regime of turbulent air-water flow through horizontal pipes. *International Journal of Multiphase Flow*, 29:1451–1471, 2003.

M. C. Roco and N. Balakrishnan. Modeling slurry flow, the effect of particle size. *Journal of Rheology*, 29(4):431–456, 1983.

M. C. Roco and S. Mahadevan. Modeling slurry flow, the effect of particle size. *Journal of Energy Resources Technology*, 108:269–283, 1986.

M. C. Roco and C. A. Shook. Modeling slurry flow, the effect of particle size. *Canadian Journal of Chemical Engineering*, 61(4):494, 1983.

M. C. Roco and C. A. Shook. A model for turbulent slurry flow. *Journal of Pipelines*, 4:3–13, 1984.

M. C. Roco and C. A. Shook. Turbulent flow of incompressible mixtures. *Journal of Fluids Engineering*, 107:224, June 1985.

R. S. Sanders, G. Halferdahl, and C. A. Shook. Correlation of slurry sedimentation, transport and deposition for oil sand tailings. In *Proc. 11th Int. Conf. Transport and Sedimentation of Solid Particles, Ghent, Belgium*, pages 299–307, September 2002.

R. S. Sanders, M. M. Razzaque, J. Schaan, K. Nandakumar, J. H. Masliyah, A. Afacan, and S. Liu. Bubble size distributions for dispersed air-water flows in a 100

Reproduced with permission of the copyright owner. Further reproduction prohibited without permission.

mm horizontal pipeline. *Canadian Journal of Chemical Engineering*, 82:858–864, August 2004.

S. C. Saxena, D. Patel, D. N. Smith, and J. A. Ruether. An assessment of experimental techniques for the measurement of bubble size in a bubble slurry reactor as applied to indirect coal liquefaction. *Chemical Engineering Communications*, 63:87–127, 1988.

J. Schaan, R. J. Sumner, R. G. Gillies, and C. A. Shook. The effect of particle shape on pipeline friction for newtonian slurries of fine particles. *Canadian Journal of Chemical Engineering*, 78:717–725, 2000.

U. Schaflinger, A. Acrivos, and K. Zhang. Viscous resuspension of a sediment within a laminar and stratified flow. *International Journal of Multiphase Flow*, 16(4):567–578, 1990.

J. S. Shirolkar, C. F. M. Coimbra, and M. Queiroz McQuay. Fundamental aspects of modeling tuburlent particle dispersion in dilute flows. *Prog. Energy Combust. Sci.*, 22:363–399, 1996.

C. A. Shook and S. M. Daniel. Flow of suspensions of solids in pipeline: I. flow with a stable stationary deposit. *Canadian Journal of Chemical Engineering*, 43 (2):56–65, 1965.

C.A. Shook and M.C. Roco. *Slurry Flow: Principles and Practice*. Butterworth-Heinemann, 1991.

C.A. Shook, R.G. Gillies, and R.S. Sanders. *Pipeline Hydrotransport with Applications to Oil Sand Industry*. SRC Publication, Saskatoon, SK, 2002.

Y. Tsuji, Y. Morikawa, and H. Shiomi. Ldv measurements of air−solid two−phase flow in a vertical pipe. *Journal of Fluid Mechanics*, 139:417–434, 1984.

J. Y. Tu and C. A. J. Fletcher. An improved model for particulate turbulence modulation in confined two phase flows. *International Communication of Heat Mass*, 21:775–783, 1994.

Reproduced with permission of the copyright owner. Further reproduction prohibited without permission.

J. P. Tucker, D. A. Deglon, J.-P. Franzidis, M.C. Harris, and C. T. O'Connor. An evaluation of a direct method of bubble size distribution measurement in a laboratory batch flotation cell. *Minerals Engineering*, 7(5/6):667–680, 1994.

G.B. Wallis. *One-dimensional Two-phase Flow*. McGraw-Hill, New York, NY, 1969.

V. Wallwork. *An Investigation of Oil Sand Processibility*. M.Sc. Thesis, University of Alberta, Edmonton, AB, 2003.

I. C. Walton. Eddy diffusivity of solid particles in turbulent liquid flow in a horizontal pipe. *AIChE Journal*, 41(7):1815–1820, 1995.

K. C. Wilson and A. Sellgren. Interaction of particles and near-wall lift in slurry pipelines. *Journal of Hydraulic Engineering*, 129(1):73–76, January 2003.

Z. Yuan and E. E. Michaelides. Turbulence modulation in particulate flows-a theoretical approach. *International Journal of Multiphase Flow*, 18(5):779–785, 1992.

K. Zhang and A. Acrivos. Viscous resuspension in fully developed laminar pipe flows. *International Journal of Multiphase Flow*, 20(3):579–591, 1994.

Reproduced with permission of the copyright owner. Further reproduction prohibited without permission.

Appendix A

Matlab code used for Image Processing

Listing A.1: MATLAB Codes Used in Image Processing

```
% The following code is used to convert from grayscale
% image to black and white from photographic technique

S='Sample.jpg';
    % This reads the image Sample.jpg
I=imread(S);
I1=imcomplement(I);
I2=imcomplement(imsubtract(I1,B1));
    % Subtracts the background image from sample
I4=medfilt2(I2,[3 3]);
    % Removes the noise
level=graythresh(I4);
I5=imadjust(I4,[level-0.2 1], []) ;
    % Gives a better contrast to the bubble edges
bwlevel = graythresh(I5);
    % Black and white level is chosen by Matlab command
I6=im2bw(I5,bwlevel);
    % Grayscale Image converted to Black and White
I7 = imfill(imcomplement(I6),'holes');
    % Incomplete holes are filled in
L=bwlabel(I7);
    % All the holes of Black and White image are
    % labelled
L_props=regionprops(L,'Area');
    % Area of holes are selected
ar=[L_props.Area];
    % Area of the bubbles and labelled image are saved
s=[S1,num2str(i)];
```


Reproduced with permission of the copyright owner. Further reproduction prohibited without permission.

```
save(s,'L','ar');

% The following code is used to view the images and
% scan the bubbles after the grayscale images have
% been converted into black and white images.
S=[S1,num2str(i)];
    % Saved Image and Area of bubbles are loaded
load('Sample.mat');
imshow(L);
    % Sample image is displayed
DesAr=sort(ar,'descend');
    % Area is sorted in descending order
MaxDesCnt=30;
if length(DesAr)<30
  MaxDesCnt=length(DesAr);
end
    % MaxDesCnt is set to 30 or to the number of
    % holes in the image depending on which is smaller
for(DesCnt=1:MaxDesCnt)
    ind=find(ar==DesAr(DesCnt));
    for(CntInd=1:length(ind))
        text(round(max(find(L==ind(CntInd)))/420)+10,...
            mod(max(find(L==ind(CntInd))),420),...
            num2str(ar(ind(CntInd))),'Color','r')
    end
end
    % Area of MaxDesCnt largest holes are displayed
        % besides the holes
close()
```


Reproduced with permission of the copyright owner. Further reproduction prohibited without permission.

Appendix B

Model Equations and Parameters

B.1 Model Equations

B.1.1 Momentum Balance

X-Direction Momentum Balance:

$$\mathrm{Re}(1+\rho_d\Phi)[u_1\frac{\partial u_1}{\partial x_1}+u_2\frac{\partial u_1}{\partial x_2}] = \frac{\partial}{\partial x_1}[\alpha\mathrm{Re}\nu_{ts}(\frac{\partial u_1}{\partial x_1}+\frac{\partial u_2}{\partial x_2})+2\nu_{ts}\frac{\partial u_1}{\partial x_1}] + \frac{\partial}{\partial x_2}[\nu_{ts}(\frac{\partial u_1}{\partial x_2}+\frac{\partial u_2}{\partial x_1})] \quad \text{(B.1)}$$

Y-Direction Momentum Balance:

$$\mathrm{Re}(1+\rho_d\Phi)[u_1\frac{\partial u_2}{\partial x_1}+u_2\frac{\partial u_2}{\partial x_2}] = \frac{\partial}{\partial x_2}[\alpha\mathrm{Re}\nu_{ts}(\frac{\partial u_1}{\partial x_1}+\frac{\partial u_2}{\partial x_2})+2\nu_{ts}\frac{\partial u_2}{\partial x_2}] + \frac{\partial}{\partial x_1}[\nu_{ts}(\frac{\partial u_1}{\partial x_2}+\frac{\partial u_2}{\partial x_1})] - \frac{\Phi}{\mathrm{Fr}} \quad \text{(B.2)}$$

Z-Direction Momentum Balance:

$$\mathrm{Re}(1+\rho_d\Phi)[u_1\frac{\partial u_3}{\partial x_1}+u_2\frac{\partial u_3}{\partial x_2}] = \frac{\partial}{\partial x_1}[\nu_{ts}\frac{\partial u_3}{\partial x_1}]+\frac{\partial}{\partial x_2}[\nu_{ts}\frac{\partial u_3}{\partial x_2}]+\mathrm{K} \quad \text{(B.3)}$$

where, ν_{ts} is as follows:

$$\nu_{ts} = \nu_{tf}\times\nu_{tm}\times\nu_{tp}\times\mathrm{Fr}_s^{b_5} \quad \text{(B.4a)}$$

$$\nu_{tf} = b_{10}Re^{0.8226} \quad \text{(B.4b)}$$

$$\nu_{tm} = e^{-\Phi_{avg}/\Phi_m} \quad \text{(B.4c)}$$

$$\nu_{tp} = 1+b_1\Phi^{b_2}+\frac{b_3}{((\Phi_m/\Phi)^{1/3}-1)^2}+b_4\frac{d\Phi}{dy} \quad \text{(B.4d)}$$

Reproduced with permission of the copyright owner. Further reproduction prohibited without permission.

B.1.2 Scalar Transport of Particles

$$[u_1\frac{\partial\Phi}{\partial x_1}+u_2\frac{\Phi}{\partial x_2}] = \frac{\partial}{\partial x_1}[D_{tpx1}\frac{\partial\Phi}{\partial x_1}]+\frac{\partial}{\partial x_2}[D_{tpx2}\frac{\partial\Phi}{\partial x_2}+N_G] \quad \text{(B.5)}$$

$$D_{tpx1} = b_8 Re^{b_9}\times \text{IE}\times(b_6 e^{-\Phi/\Phi_m}+\frac{b_7}{((\Phi_m/\Phi)^{1/3}-1)^2}) \quad \text{(B.6a)}$$

$$D_{tpx2} = b_8 Re^{b_9}\times \text{CTE}\times \text{IE}\times(b_6 e^{-\Phi/\Phi_m}+\frac{b_7}{((\Phi_m/\Phi)^{1/3}-1)^2}) \quad \text{(B.6b)}$$

$$\text{IE} = \frac{1}{\sqrt{1+\frac{\tau_p}{T_L}}} \quad \text{(B.6c)}$$

$$\text{CTE} = \frac{1}{\sqrt{1+(\frac{10g\tau_p T_L}{D_t})^2}} \quad \text{(B.6d)}$$

$$N_G = \frac{2}{9}(\frac{d_p}{L})^2\frac{1}{Fr}\Phi f(\Phi) \quad \text{(B.6e)}$$

$$f = \frac{1-\Phi}{\mu_r} \quad \text{(B.6f)}$$

$$\mu_r = (1+\frac{1.5\Phi}{1-\frac{\Phi}{\Phi_m}})^2 \quad \text{(B.6g)}$$

B.2 Fitted Parameters

Parameter	Value
b_1	10.30
b_2	0.70
b_3	0.08
b_4	5.00
b_5	0.13
b_6	1.00
b_7	0.06
b_8	7.81
b_9	(-)0.20
b_{10}	1.44×10^{-3}
α	1000

Table B.1: Model Parameters

Reproduced with permission of the copyright owner. Further reproduction prohibited without permission.